Comprehensive Model Simulation of Thermal Tides in the Martian Atmosphere

R. JOHN WILSON AND KEVIN HAMILTON

Geophysical Fluid Dynamics Laboratory/NOAA, Princeton University, Princeton, New Jersey

(Manuscript received 20 June 1995, in final form 30 October 1995)

ABSTRACT

This paper discusses the thermotidal oscillations in simulations performed with a newly developed comprehensive general circulation model of the Martian atmosphere. With reasonable assumptions about the effective thermal inertia of the planetary surface and about the distribution of radiatively active atmospheric aerosol, the model produces both realistic zonal-mean temperature distributions and a diurnal surface pressure oscillation of at least roughly realistic amplitude. With any reasonable aerosol distribution, the simulated diurnal pressure oscillation has a very strong zonal variation, in particular a very pronounced zonal wavenumber-2 modulation. This results from a combination of the prominent wave-2 component in the important boundary forcings (topography and surface thermal inertia) and from the fact that the eastward-propagating zonal wave-1 Kelvin normal mode has a period near 1 sol (a Martian mean solar day of 88 775 s). The importance of global resonance is explicitly demonstrated with a series of calculations in which the global mean temperature is arbitrarily altered. The resonant enhancement of the diurnal wave-1 Kelvin mode is predicted to be strongest in the northern summer season. In the model simulations there is also a strong contribution to the semidiurnal tide from a near-resonant eastward-propagating wave-2 Kelvin mode. It is shown that this is significantly forced by a nonlinear steepening of the diurnal Kelvin wave. The daily variations of near-surface winds in the model are also examined. The results show that the daily march of wind at any location depends strongly on the topography, even on the smallest horizontal scales resolved in the model ($\sim$ few hundred km). The global tides also play an important role in determining the near-surface winds, especially so in very dusty atmospheric conditions.

The results for the diurnal and semidiurnal surface pressure oscillations in seasonal integrations of the model are compared in detail with the observations at the two Viking Lander sites (22°N and 48°N). The observations over much of the year can be reasonably reproduced in simulations with a globally uniform aerosol mixing ratio (and assuming more total aerosol in the northern winter season, when the largest dust storms are generally observed). There are features of the Viking observations that do not seem to be explainable in this way, however. In particular, in early northern summer, the model predicts amplitudes for the diurnal pressure oscillation at both lander sites that are at least a factor of 2 larger than observed. Results are presented showing that the low amplitudes observed could be explained if the dust distribution tended to be concentrated over the highlands, rather than being uniformly mixed. Annual cycle simulations with a version of the model with an interactive dust transport do in fact reveal the tendency of the circulation to organize so that larger dust mixing ratios occur over highlands, particularly near subsolar latitudes. When the model includes globally uniform surface dust injection and parameterized dust sedimentation, the annual cycle of the diurnal and semidiurnal tides at both lander sites can be rather well reproduced, except for the periods of global dust storms. The attempts to simulate the observed rapid evolution of the tidal pressure oscillations during the onset of a global dust storm also demonstrate the importance of a nonuniform dust concentration. Simulations with the version of the model incorporating interactive dust are able to roughly reproduce the Viking observations when a strong zonally uniform dust injection is prescribed in the Southern Hemisphere Tropics and subtropics.

1. Introduction

The dynamical response to the diurnal heating on a rapidly rotating planet is expected to be inversely proportional to the mean density. Since the total column mass of the atmosphere on Mars is about two orders of magnitude less than that on earth, the thermally forced solar tidal variations should represent a much more important component of the circulation in the Martian atmosphere than in the terrestrial atmosphere. This expectation has been borne out in both in situ near-surface observations (e.g., Zurek and Leovy 1981) and remotely sensed temperature measurements (Conrath et al. 1973). Theoretical calculations suggest that the tides may be strong enough to play a significant role in determining the zonally averaged circulation of the Martian atmosphere (e.g., Hamilton 1982). Tidal winds are also likely to contribute significantly to the lifting and transport of dust in the atmosphere (e.g., Leovy and Zurek 1979).

One intriguing aspect of tides on Mars is the possibility that the diurnal forcing may resonate with a global normal-mode oscillation of the atmosphere. The

Corresponding author address: Mr. R. John Wilson, Geophysical Fluid Dynamics Laboratory, NOAA, P.O. Box 308, Princeton, NJ 08542.

idea of an astronomically forced atmospheric resonance has a long history, having been first introduced in the last century by Lord Kelvin as a possible explanation for the prominence of the semidiurnal tide in the terrestrial atmosphere (Thompson 1882). While this speculation is now known to be incorrect (e.g., Chapman and Lindzen 1970), it helped stimulate the development of the theory of both atmospheric tides and normal modes. For the Martian atmosphere, the issue of resonance was first raised in the linear forced tidal calculations of Zurek (1976), who noted the possibility that the gravest zonal wavenumber 1 eastward-propagating tidal component on Mars could be resonantly amplified. Hamilton (1984) and Hamilton and Garcia (1986) examined long time series of observations in the terrestrial atmosphere and found evidence for a wavenumber-1 normal-mode equatorial Kelvin wave, analogous to the familiar "five-day" Rossby normal mode (Madden 1978; Salby 1981a,b). In the terrestrial atmosphere, this Kelvin mode has a period near 33 h and hence is well removed from the diurnal forcing frequency. Hamilton and Garcia performed simple calculations that suggested that in the Martian atmosphere the period for the same normal-mode Kelvin wave should be close to one day. Since the primary forcing for the solar tide is sun-synchronous (i.e., westward propagating), the generation of diurnal excitation for this Kelvin mode requires zonal inhomogeneities in either the distribution of local time heating rates or in the lower boundary. The topographic relief on Mars is very large, and so may contribute to a strong forcing for the non-sun-synchronous tidal components. Zurek (1988) reexamined the issue of the possible resonance of the wavenumber-1 normal-mode Kelvin wave with the diurnal forcing. He again considered this in the context of simplified linear theory and concluded that resonant amplification could be important for the tide in at least part of the Martian annual cycle.

To date, the published theoretical treatments of Martian tides have all used linear theory with simplified mean states and either no topography or treatments of the topographic lower boundary condition involving some approximation (Conrath 1976; Zurek 1976). The present paper will examine the thermal tides in a comprehensive, nonlinear general circulation model (GCM) with an exact treatment of the lower boundary condition appropriate for finite-amplitude topography. The model also includes nonlinear radiative transfer and vertical mixing parameterizations. An extensive set of calculations with a version of the model using prescribed atmospheric dust concentration (which largely determines the thermotidal forcing) will be described, with an emphasis on (i) establishing the relevance of global resonance for the diurnal and semidiurnal thermotidal response, (ii) investigating the role of the topographic relief and other sources of excitation for the resonant eastward-moving tide, and (iii) determining the assumptions that need to be made concerning the dust distribution in order for the model to account for the detailed seasonal cycle of the tides (as observed in the surface pressure). The model is then extended to include a prognostic equation for the dust concentration. It will be shown that many of the features observed in the seasonal evolution of the tides can be captured in model integrations with plausible prescribed sources of surface injection of dust into the atmosphere.

The plan of this paper is as follows. Section 2 briefly reviews the basic theory of tides and normal modes. Section 3 discusses the available observations and previous theoretical calculations of Martian tidal fields. Section 4 provides a detailed description of the present Martian atmospheric model. Some basic features of the simulated general circulation obtained with this model are outlined in section 5. Section 6 discusses the results for the atmospheric tides in the model. Conclusions are summarized in section 7.

2. Brief review of theory of tides and normal modes

The so-called classical theory of atmospheric tides and normal modes considers disturbances that are described by primitive equations linearized about a motionless mean state with temperature a function only of height (e.g., Chapman and Lindzen 1970). Full spherical geometry is included, but no topography is allowed at the lower boundary. Assuming solutions that are sinusoidal in time and in the zonal direction, one finds that the meridional and vertical structures are separable. The meridional structure is governed by the Laplace tidal equation (LTE) with the well-known Hough function solutions. In tidal theory one considers the response to a known monochromatic thermal excitation. The forcing at each height can be decomposed into the appropriate Hough functions. Then for each Hough function considered, one solves a vertical structure equation, which is a second-order equation with the projection of the diurnal (or higher harmonic) heating as an inhomogeneous term. The vertical structure equation includes the separation constant for the particular Hough mode, which is obtained as part of the solution of the homogeneous LTE and which is conventionally expressed in terms of an equivalent depth, h. The nature of the Hough mode solutions for the diurnal and semidiurnal tides has been studied extensively for the terrestrial atmosphere (e.g., Chapman and Lindzen 1970) and most of the general conclusions are expected to apply as well to the Martian atmosphere (e.g., Lindzen 1970). The direct solar forcing tends to be concentrated in sun-synchronous components (westward-propagating zonal wavenumbers 1 and 2 for the diurnal and semidiurnal tides, respectively). The semidiurnal tidal response in the sun-synchronous wave is dominated by a broad equatorially trapped Hough mode that is associated with a very long vertical wavelength and thus is particularly efficiently excited by vertically ex-

tended forcing (such as that resulting from the ozone heating in the terrestrial atmosphere). There is little phase propagation in this dominant mode, and this means that the calculated semidiurnal surface pressure oscillation [$S_2(p)$ in the usual notation, e.g., Chapman and Lindzen 1970] is found to peak near 0900 local solar time if the forcing peaks at local noon. The sun-synchronous diurnal tidal response is more complicated, with vertically propagating modes of rather short vertical wavelength dominating at low latitudes and vertically trapped modes dominating poleward of about 30° lat. The predicted phase of $S_1(p)$ in the extratropics is very close to 0600 local time for heating that peaks at local noon. The expected phase is earlier in the Tropics and can be sensitive to the depth of the heating.

The non-sun-synchronous components of the tide can be forced by zonal inhomogeneities in atmospheric absorber concentration or in the surface properties (heat capacity, soil moisture) that control the diurnal cycle of convective heating in the atmosphere. Zonally varying topography can also force non-sun-synchronous components. The net effect of these zonal variations is to modulate the sun-synchronous forcing. In the case of the diurnal tide, for example, zonal wavenumber-2 inhomogeneities in the lower boundary will force the westward propagating wavenumber-3 and eastward propagating wavenumber-1 tidal components. For the semidiurnal tide, wavenumber-4 inhomogeneities in the lower boundary force the westward propagating wavenumber-6 and eastward propagating wavenumber-2 components. In the terrestrial atmosphere these non-sun-synchronous components are more than an order-of-magnitude weaker than those that follow the sun (at least at low and midlatitudes).

One can use the classical formalism to investigate the free oscillations of the atmosphere. If the forcing in the vertical structure equation is set to zero, then the solutions determine the values of h for which resonance is possible. The corresponding LTE describes the possible free oscillations of a barotropic fluid of mean depth h. When reasonable terrestrial parameters are used, the only solution to the vertical structure equation is for $h \sim 10$ km and corresponds to the familiar equivalent barotropic Lamb wave (e.g., Chapman and Lindzen 1970; Salby 1984). The solutions of the homogeneous LTE in this case fall into the familiar type 1 (Rossby) modes and type 2 (gravity and equatorial Kelvin) modes (Longuet-Higgins 1968). Each normal-mode solution to this LTE has a different frequency and so the fact that $h \sim 10$ km solves the homogeneous vertical structure equation implies a predicted normal-mode spectrum consisting of many discrete lines.

The relevance of the simple classical theory of resonant normal modes for the terrestrial atmosphere has been examined rather extensively for the Rossby modes. Salby (1981a,b, 1984) has considered the forced linear response of an atmosphere with dissipation and realistic zonal mean states. While Salby found very significant deviations from classical theory, he concluded that the classical theory is still a useful guide and that the gravest few Rossby modes of low zonal wavenumber should be identifiable in the terrestrial atmosphere [and, in fact, a number of such modes have been found in data (e.g., Hirota and Hirooka 1984, 1985)]. The classical theory should be even more useful for the (higher frequency) gravity and Kelvin normal modes. Indeed Hamilton and Garcia (1986) analyzed terrestrial data and detected clear spectral peaks near the predicted frequencies of several of the classical gravity and Kelvin modes. However, the issue of applicability of the classical theory to the same modes on Mars is complicated by the lower phase velocities predicted for the normal modes (for the wavenumber-1 Kelvin wave ~ 240 m s^{-1} on Mars versus ~ 340 m s^{-1} on the earth), the larger atmospheric radiative dissipation, the greater strength of the diurnal forcing, and the larger topographic relief. Also distinguishing the Martian and terrestrial tidal problems are the much larger seasonal and interannual variability of the Martian zonal-mean winds and temperatures due to the variable nature of atmospheric aerosols and the eccentricity of the Martian orbit. (The solar insolation is 44% smaller at aphelion than at perihelion.)

3. Review of observations and earlier calculations of Martian tidal fields

a. Observations and classical tidal theory calculations of tidal pressure variations

The data provided by the surface landers of the NASA Viking Mission represent a unique resource for the investigation of planetary atmospheres. The study of Martian tides has been greatly facilitated by the time series of observations of near-surface (1.6 m) pressure, temperature, and horizontal wind made by the *Viking 1* (VL1, 22.5°N, 48°W) and *Viking 2* (VL2, 48°N, 134°E) landers. The surface pressure records are particularly extensive (nearly four Martian years at *Viking 1*). Zurek et al. (1992) review aspects of the low-frequency variability in these records, notably the large seasonal variation in surface pressure associated with the condensation and sublimation of the CO_2 ice caps, and the 2–10-day period oscillations in the autumn, winter, and spring seasons reflecting the presence of eastward-propagating baroclinic waves. In addition, the tidal oscillations in the Viking surface pressure observations have been extensively discussed (e.g., Hess et al. 1977; Leovy 1981; Leovy and Zurek 1979; Zurek and Leovy 1981; Leovy et al. 1985). Figure 1 shows the observations of the amplitude and phase of $S_1(p)$ at each of the two landers. Figure 2 shows the comparable results for $S_2(p)$. Each plotted point in these figures represents a phase or amplitude determination from a simple harmonic analysis of the data, typically spanning a period of a few sols. See the appendix for

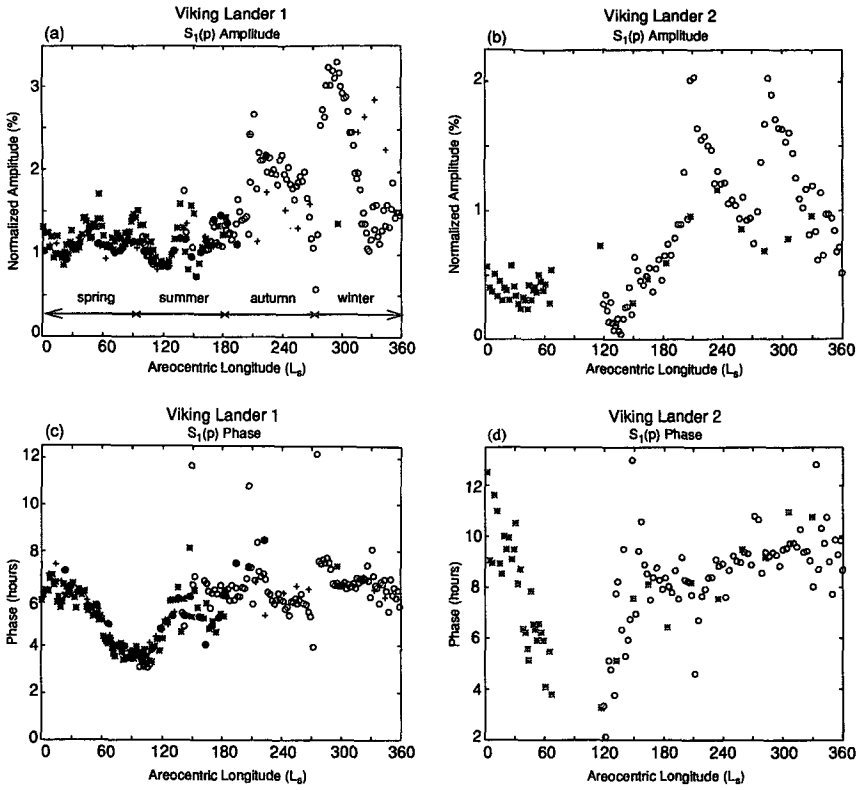

FIG. 1. The amplitude (top) and phase (bottom) of $S_1(p)$ at Viking Lander 1 (left) and Viking Lander 2 (right). Results are expressed as functions of areocentric longitude and are plotted for the first Martian year of the Viking mission (open circles), the second year (stars), the third year (crosses), and the fourth year (filled circles). The amplitudes are expressed as percent of the mean pressure, and phases are the local time of maximum pressure in the diurnal harmonic. The arrows in the top left panel show the duration of the seasons in the Northern Hemisphere (NH). Local times are such that 0000 and 1200 refer to midnight and noon, respectively.

further details. The results are displayed as a function of time of year that is represented by the areocentric longitude, L_s, defined to be zero at the vernal equinox, 90° at Northern Hemisphere (NH) summer solstice, etc. These plots of the Viking data are similar to others that have appeared in earlier publications (e.g., Leovy 1981); however, Figs. 1 and 2 are the first to summarize results for all available years of Viking pressure tidal data in a single panel.

Apart from episodic events, the phases of $S_1(p)$ and $S_2(p)$ undergo a regular annual cycle, with a similar trend apparent at both landers. Especially prominent is the rapid advance and subsequent lag in phase of $S_1(p)$ as the year progresses through NH summer solstice (L_s = 90). The interannual variability in $S_1(p)$ and $S_2(p)$ is not particularly pronounced in NH late spring and summer. This early phase is not predicted by classical tidal theory for either latitude. Tillman (1988) has documented and discussed the presence of transient changes in the phase and amplitude of the tides at the two landers in late summer (L_s = 140–150). By contrast, there is considerable interannual variability in the tidal signals during the period from early autumn through winter, when most of the significant dust storms are known to occur (e.g., Martin and Zurek 1993). There are two very large, sharp spikes in the amplitude of $S_2(p)$ during the first year at VL1 corresponding to the 1977a and 1977b planet-encircling dust storm events (e.g., Leovy and Zurek 1979). It is known that these two events were each accompanied by comparably sharp increases in atmospheric total optical depth and decreases in the diurnal range of near-surface temperature. A similarly intense episode is apparent in the fourth year of the $S_2(p)$ record (Leovy et al. 1985; Tillman 1988). These dust storm events are also evident in the $S_1(p)$ signal at both lander sites. Classical tidal theory applied to the sun-synchronous components has been shown to at least roughly account for the amplitudes of the observed oscillations during this season (Zurek and Leovy 1981; hereafter ZL). In particular, ZL demonstrated that classical tidal theory can reproduce the observed dependence of the strength of the semidiurnal tide on aerosol optical depth. The calculated phases are not in such good agreement, how-

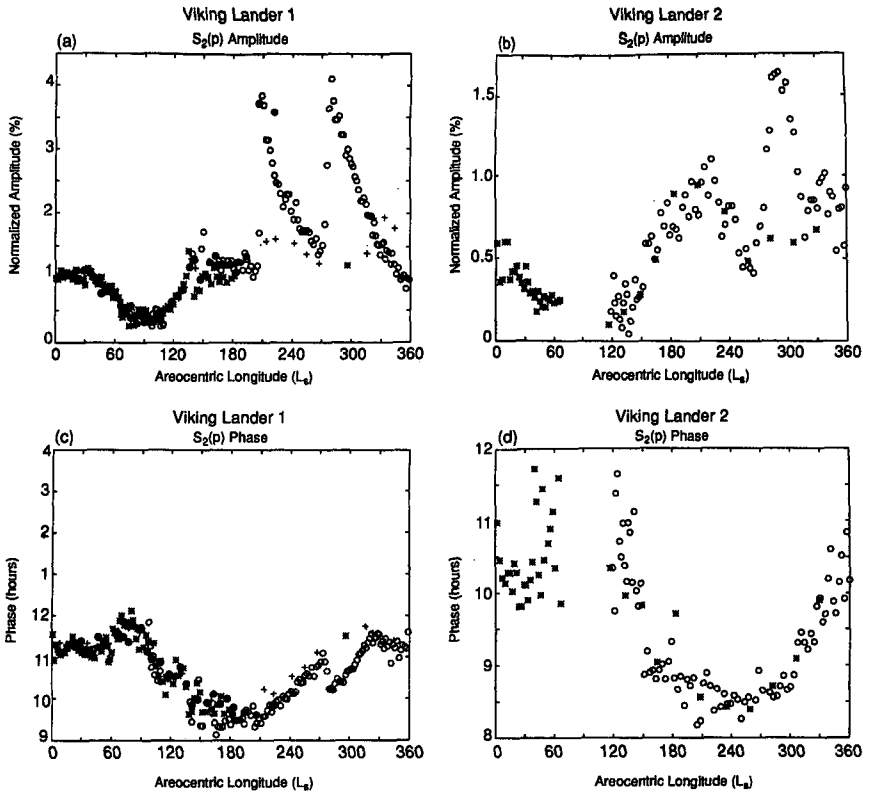

FIG. 2. As in Fig. 1 but for $S_2(p)$.

ever. Zurek and Leovy computed $S_2(p)$ phases for both lander sites that are too early and have a seasonal trend opposite that observed. For VL1 the calculated phase of ZL for $S_1(p)$ is roughly correct but is very insensitive to changing optical depth and so does not capture the observed $S_1(p)$ phase variability during the dust storms. The corresponding phase at VL2 is about 2–3 h earlier than observed.

There was a notable drop in the amplitude of $S_1(p)$ at VL1 just prior to the start of the 1977b dust storm. Associated with this drop (and subsequent increase) in amplitude was an advance (and then lag) of the phase. Zurek and Leovy commented that this behavior could be explained by a rapid enhancement of a topographically induced eastward-traveling diurnal tidal component that destructively interferes with the classical westward-traveling tide at the Viking Lander sites. They proposed that enhanced heating over highlands could excite a Kelvin wave with appropriate phase to account for the near cancellation of $S_1(p)$ at VL1.

The influence of the state of the atmospheric aerosol distribution on the tides is apparent in the Viking pressure observations. A good overview of the Martian dust cycle is given by Kahn et al. (1992). Visible optical depths directly measured at the two Viking landers indicate base values of 0.3–0.5 present throughout the Martian year. Values of unity (or substantially greater), with episodic variability, were reported from NH autumn through winter (L_s = 180–360).

Atmospheric temperatures derived from spacecraft observations have also indicated the presence of significant diurnal tides. Temperature data obtained from *Mariner 9* infrared interferometer spectrometer (IRIS) observations following the 1971 global dust storm offer evidence for strong aerosol heating up to 50 km in height and resulting large-amplitude (30 K peak to peak) diurnal thermal tides (Hanel et al. 1972). This instrument has a vertical resolution of roughly half a scale height (~10 km). Diurnal tidal amplitudes were also derived from *Viking Orbiter* infrared thermal mapper (IRTM) observations and are presented by Martin and Kieffer (1979). The IRTM reported 15-μ brightness temperatures for a thick layer of atmosphere centered at approximately 0.5 mb (~25 km). Tidal amplitudes of 10–15 K were observed following the two 1977 dust storms, with peak amplitudes at middle to high latitudes in the Southern (summer) Hemisphere.

Conrath (1976) plotted 2-mb level IRIS temperatures (for 1600–1700 and 0600–0700 LT) versus longitude for three latitude intervals in the Southern (summer) Hemisphere. He found that the longitudinal variation in the amplitude of the diurnal temperature range was significant and proposed that this behavior might result from topographic modulation of the thermal tide.

b. Previous tidal calculations including topography

Conrath (1976) considered perhaps the simplest possible generalization of classical theory to include topographic effects. He estimated the amplitude of the sun-synchronous diurnal tide on the basis of *Mariner 9* IRIS remotely sensed atmospheric temperatures. Classical tidal theory was used to deduce the diurnal surface winds associated with this temperature signal. The vertical velocity associated with these winds was then used as a linearized lower boundary condition in the vertical structure equation for each Hough mode describing the perturbation response. Conrath found that the most prominent of the expected non-sun-synchronous modes was a near-resonant eastward propagating zonal wavenumber 1 Kelvin wave excited by the zonal wavenumber 2 topography. Conrath found that the temperature perturbation associated with the predicted non-sun-synchronous component was roughly consistent with his IRIS observations.

Zurek (1976) developed a formulation for more completely incorporating the effects of topography. While still employing a motionless mean state and a linearized version of the lower boundary condition, Zurek considered the full coupling that is induced among different classical tidal modes. Thus, his model requires the specification of the thermal tidal drive and then involves the simultaneous solution of a number of coupled vertical structure equations. In his formulation, Zurek was able to distinguish between dynamically induced topographic effects and effects of the longitudinal distortions of boundary layer heating expected to be caused by topography. Zurek implemented his model for a rather severely truncated set of Hough modes (five modes for the sun-synchronous component plus a total of four more modes describing westward propagating wave 3 and eastward propagating waves 1 and 3). For realistic topography and a representative "clear-sky" temperature profile, Zurek found that the zonal wave-1 Kelvin mode should be a very prominent component of the tidal response.

Zurek repeated his calculations for various temperature profiles and found a strong dependence of the Kelvin wave response on the near-surface static stability. In particular, the dynamical effects of the wave 2 topography become increasingly effective at exciting the Kelvin wave as the near-surface lapse rate approaches being adiabatic.

c. Diurnal variability of surface winds

The daily variability of the surface winds measured by the Viking landers has been discussed by Hess et al. (1977), Leovy and Zurek (1979), Leovy (1981), and Murphy et al. (1990). There are wind observations for two Martian years at VL2 but only one year at VL1. The interpretation of the wind data is complicated by the contamination of the global tidal signal by regional and local effects induced by topography and other inhomogeneities in the lower boundary (e.g., Blumsack et al. 1973). In fact, in the terrestrial atmosphere, little agreement has been found between the observed diurnal cycle of surface winds and that expected from linear tidal theory (Chapman and Lindzen 1970). Hess et al. (1977) discuss hodographs of the Viking lander winds corresponding to early NH summer. At this time the VL1 winds exhibited a counterclockwise rotation through the day with a phase such that winds were directed downslope during the morning and upslope during the afternoon. Linear theory for the sun-synchronous component of the tide predicts a clockwise rotation of the horizontal surface wind through the day in the NH. Hess et al. explained the sense of rotation of the early summer VL1 observations by postulating a diurnal modulation of turbulent mixing whereby strong afternoon mixing couples the surface winds to the observed (Seiff 1993) southerly winds aloft. In late summer the observed winds at VL1 began to exhibit clockwise rotation through the day. Since the winds aloft are expected to switch to northerly as the Hadley circulation migrates southward with the subsolar latitude, this change in the diurnal surface wind variation may also be explained by the diurnal modulation of mixing (Murphy et al. 1990). Murphy et al. found that at neither lander was the phase of $S_1(u)$ or $S_1(v)$ consistent with that expected of a westward propagating diurnal tide, even during global dust storms when the tidal forcing was particularly strong.

Simulations of the diurnal wind cycle expected at the Viking sites for the summer season have been carried out using simple limited-area models incorporating slope effects (Savijarvi and Silli 1993; and Haberle et al. 1993b). Their models provide for an imposed constant geostrophic wind but do not account for propagating global-scale tides. These studies have been able to reproduce some of the observed wind characteristics, notably the sense of wind rotation at each site. However, the results show a strong sensitivity to the local topographic slope employed.

During the late autumn and winter seasons, when the aerosol loading is larger, daily hodographs at both lander sites were found to be dominated by a semidiurnal variation. For this period Leovy and Zurek (1979) and Leovy (1981) showed that the observed VL2 semidiurnal wind components were consistent in phase and amplitude with a sun-synchronous $S_2(p)$ signal of the observed strength. Murphy et al. (1990) demonstrated this to be the case at VL1 as well.

4. Model description

Comprehensive general circulation modeling of the Martian atmosphere began with the two-level model described in Leovy and Mintz (1969). Later developments of this model were made at NASA Ames Research Center and are described in Pollack et al. (1981;

1990). More recently, a Martian general circulation model has been adapted from a terrestrial climate model at the Laboratoire de Meteorologie Dynamique and is described by Hourdin et al. (1993). The present project involved the development of a comprehensive Martian GCM, which in many ways is similar to the most recent version of the Ames model. In this section some of the basic features of the present model formulation will be described.

a. Dynamics

This three-dimensional Martian simulation model has been developed from the GFDL SKYHI terrestrial GCM (Fels et al. 1980; Mahlman and Umscheid 1987; Hamilton et al. 1995). As in SKYHI, the full nonlinear primitive equations are discretized on a nonstaggered latitude–longitude grid by means of the box method (Kurihara and Holloway 1967). At high latitudes a Fourier filter is applied to enforce an approximately uniform longitudinal scale for the effective horizontal resolution. An explicit leapfrog scheme, combined with a time filter and with an Euler backward scheme applied once every 24 time steps, is used to integrate the prediction equations. The model uses a hybrid vertical coordinate system, which is terrain following near the ground and purely isobaric above approximately 2 mb. The vertical grid is staggered with temperature and horizontal wind computed on full levels and the vertical velocity on half levels. The usual "rigid lid" upper boundary condition is employed, that is, the vertical pressure velocity is set to zero at the top half level nominally at zero pressure. In most of the integrations described here, the model was run with 5° × 6° lat–long spacing. Some experiments employed 40 full model levels (L40) extending from the ground to roughly 0.06 μb (~88 km). Another version (L16) with 16 full levels up to 0.9 μb (~68 km) was also used. The positions of the levels in the two versions are shown in Fig. 3. This figure also shows the level structure in the Ames model, which is roughly comparable to that in the present L16 version. The Ames model has 13 computational levels extending up to ~47 km altitude and a 7.5° × 9° lat–long grid. The present model was integrated with either 240 or 288 time steps per Martian sol (88 775 s), and the radiation was updated every four time steps.

At present the model does not incorporate the CO_2 condensation circulation but does instantaneously adjust the air temperature anywhere it would have fallen below the condensation temperature. Haberle et al. (1993a, hereafter H93) find that the omission of the condensation circulation is not important in determining the zonal mean wind and temperature fields except at the surface in the vicinity of the polar caps (and so should not be of significance for tidal simulation). Of course the mass exchange at the polar caps is a dominant component of the annual cycle of surface pressure

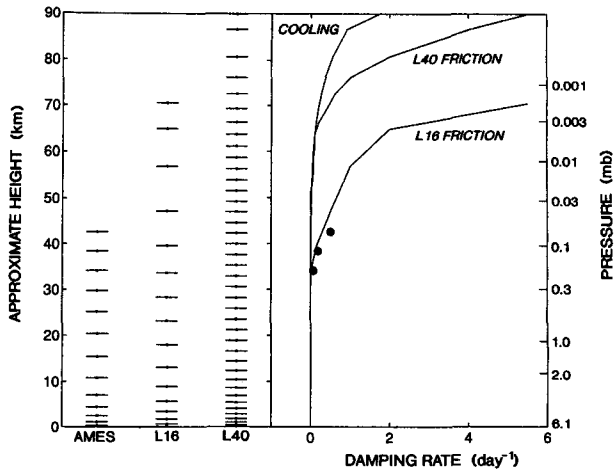

FIG. 3. (a) Model levels used in the 40-level and 16-level versions of the GCM. Those of the NASA/Ames Martian GCM are also shown. (b) Newtonian cooling and Rayleigh friction coefficients for the two model versions. The Rayleigh friction coefficients used in the top levels of the Ames GCM are shown by the dots.

so that the mass of the real Martian atmosphere varies by about 25% over the year (Zurek et al. 1992). In the simulations reported here, the global mean surface pressure is fixed at 5.14 mb. This choice of total mass leads to good agreement between the diurnal-mean pressure in the model and at the Viking landers during late NH summer when the actual atmospheric mass is least. Consequently, the model mass is a significant underestimate of the observed pressure during NH winter when the actual atmospheric mass is greatest.

The specific heat for the atmosphere used here is C_p = 770 J K^{-1} kg^{-1}, based on a mixture of 95% CO_2, 3% N_2, and 2% Ar (by volume) at 210 K (Touloukian and Makita 1970). Note that the present value differs from those used in earlier studies [e.g., 734 J K^{-1} kg^{-1} by Haberle et al. (1982) and 860 J K^{-1} kg^{-1} by Zurek et al. (1992)]. The specific heat of the atmosphere is particularly relevant for the resonant properties of the Kelvin wave. In the case of an isothermal atmosphere, the equivalent depth of the atmosphere is proportional to $(1 - R/C_p)^{-1}$.

b. Radiative transfer

Atmospheric heating due to absorption of solar radiation in the near-IR bands of CO_2 and by aerosols are both included. The shortwave dust heating is calculated using a delta-Eddington approximation for aerosol scattering (Briegleb 1992). The single scattering albedo, phase function asymmetry parameter, and extinction efficiency employed are those derived by Pollack et al. (1979) from Viking lander imaging observations of the sky and sun. These values represent an average over the solar spectrum. There is evidence (Clancy et al. 1995) that different values of these pa-

rameters may in fact be more appropriate, leading to some uncertainty in the actual solar energy deposition in the atmosphere for a given optical depth. For example, the parameters advocated by Clancy et al. result in less solar heating due to the reduced single scattering albedo and increased backscattering. The heating due to the absorption of direct solar radiation by CO_2 is computed using the scheme of Houghton (1963) as implemented by Burk (1976). The aerosol heating strongly dominates the CO_2 heating below 40 km.

The IR effects of CO_2 are calculated using the simple 15 μ CO_2 band model of Goody and Belton (1967) in the strong Lorentzian line limit. The 4.3-μ and 2.7-μ bands are neglected as unimportant at the low prevailing Martian temperatures. This scheme allows use of an analytic derivative of the transmission function, which makes the accuracy of the heating rates nearly independent of the selected vertical resolution. There is no temperature dependence in this band formulation. Hourdin (1992) has presented results from line-by-line calculations for the Martian atmosphere and developed numerical approximations for CO_2 15-μ band absorption. He showed that the Lorentz approximation can yield very accurate flux results to roughly 50 km and accurate cooling rates to even higher altitudes. Although the Lorentz line width is smaller than that of a Doppler line above about 5 mb, the Doppler core is saturated and radiative exchange occurs primarily in the Lorentzian wings. The results for the CO_2 IR cooling rates in an isothermal atmosphere calculated with the present scheme compare reasonably well with those of Hourdin (1992) up to around 45 km (largest discrepancies are near 25 km where the present calculations result in cooling rates ~30% larger than those of Hourdin). Above about 45 km, the present cooling rate asymptotes to a constant value rather than continuing to increase as in the line-by-line calculations. The agreement with the line-by-line results is also reasonable for realistic Martian temperature profiles. For a wavelike temperature perturbation, the present scheme produces even better agreement with that of Hourdin. The typical damping rate for a 20-km wavelength perturbation is ~2 sol^{-1}. Above 45 km the present scheme is supplemented by an arbitrary linear damping toward a constant temperature of 140 K. The Newtonian damping rate employed is shown as a function of pressure in Fig. 3.

Cooling by dust in the IR is computed using the emissivity formulation of Haberle et al. (1982) for the spectral region exclusive of the 15 μ band. This formulation is based on the particle size distribution inferred by Toon et al. (1977) and on the optical properties of montmorillonite 219b, a silicate mineral. This results in a ratio of visible opacity to IR (9 μ) opacity of about 1. This ratio is fairly sensitive to the dust particle size distribution as discussed by Murphy et al. (1993). A distribution emphasizing smaller particles leads to a visible to IR dust opacity ratio closer to 2.5, in accord with that inferred from *Viking Orbiter* observations (e.g., Clancy et al. 1995). The effect of dust in the 15-μ CO_2 band is neglected and so the IR opacity of the atmosphere should be somewhat underestimated, particularly for large aerosol concentrations. The aerosol cooling rates computed for a wavelike temperature perturbation become comparable with those for CO_2 when the dust concentrations (with vertically uniform mass mixing ratio) are such that the column-integrated visible optical thickness τ is near unity.

In the experiments with prescribed aerosol, the mass mixing ratio had a horizontally uniform distribution, to the extent allowed by the presence of topography. The formulation of Conrath (1975) was used to describe the dust mixing ratio as a function of pressure—that is,

$$q = q_0 \exp\left[\nu\left(1 - \frac{p_{\text{ref}}}{p}\right)\right], \qquad (4.1)$$

where ν is a constant that determines the pressure below which the mixing ratio rapidly decreases. The constants used here were $\nu = 0.01$ and $p_{\text{ref}} = 6.1$ mb, resulting in a relatively constant aerosol mixing ratio up to about 35 km. Note that Pollack et al. (1990) and H93 both used $\nu = 0.03$ and $p_{\text{ref}} = 7.6$ mb. Results here confirm their assertion that the zonal mean climate is not sensitive to the value of ν.

c. *Subgrid-scale mixing parameterizations*

A second-order vertical diffusion with Richardson-number-dependent coefficient is applied to both horizontal momentum and heat (see Levy et al. 1982; Hamilton et al. 1995). A nonlinear diffusion scheme is employed for horizontal mixing of momentum and heat (Andrews et al. 1983). The model includes a standard convective adjustment scheme that mixes heat, but not momentum, within convectively unstable regions.

d. *Dissipation in the upper atmosphere*

It was found that when the model is run with no additional dissipation, very strong zonal-mean winds develop at heights above 40 km, particularly for cases with large aerosol loading. It is unclear whether these intense simulated winds are realistic. In any case, they are not an artifact of the rigid upper lid. The standard model incorporates a linear damping of the zonal-mean wind in the upper levels in order to ensure a mean state allowing stable integrations with a reasonable time step. The values of the Rayleigh friction coefficient employed are shown in Fig. 3 as a function of pressure for both the L40 and L16 versions. Also shown for comparison are the Rayleigh friction coefficients used in the Ames model (Pollack et al. 1990). Note that the frictional damping in the Ames model is applied to local velocities and thus damps all eddies as well as the

mean flow. In the present model a linear damping with a coefficient of $(10\ 800\ \text{s})^{-1}$ is applied to all deviations from the zonal mean (for all fields) at the top full level. This acts as a crude sponge layer to reduce spurious downward wave reflections.

The treatment of the atmospheric physics above about 45 km in the present model is somewhat arbitrary. In particular, simulations have been performed for a number of different formulations of the Rayleigh friction and/or level structures in the upper atmosphere. These various versions of the model have shown that the mean meridional circulation and the zonal-mean zonal wind above about 40 km are sensitive to the strength of the damping employed. Fortunately, in all these experiments the tidal fields below about 40 km were found to be quite insensitive to the details of the simulation in the upper atmosphere.

e. Surface physics

Surface thermal inertia, ice-free albedo, roughness, and topographic height must all be specified in the model. The albedo and thermal inertia fields employed in the standard experiments were based on those of Pollack et al. (1990) and provided by R. Haberle. These fields were derived from Viking orbiter radiometer observations of the diurnal range of surface temperature by fitting to a simple surface thermal model (Kieffer et al. 1977; Palluconi and Kieffer 1981). The present GCM includes prognostic equations for the temperature in each of eight soil layers (varying in thickness from 0.3 cm for the top layer to 10 cm for the bottom layer). The model considers energy exchanges between the top soil layer and the bottom atmospheric layer and thermal diffusion between adjacent soil layers. At a particular grid point, every layer has the same specified values of heat capacity, C, thermal conductivity, K, and density, ρ. The diffusivity varies with geographical location resulting in an effective surface thermal inertia $(\rho CK)^{1/2}$ that also depends on location. In the present simulations the albedo and surface thermal inertia fields were smoothed by retaining only zonal waves 0–6. The top panel in Fig. 4 shows the distribution of thermal inertia used in the standard experiments. A rather prominent zonal wave 2 variation is evident. Figures 4b and 4c display the zonal wavenumber 2 and 4 components of this field, respectively.

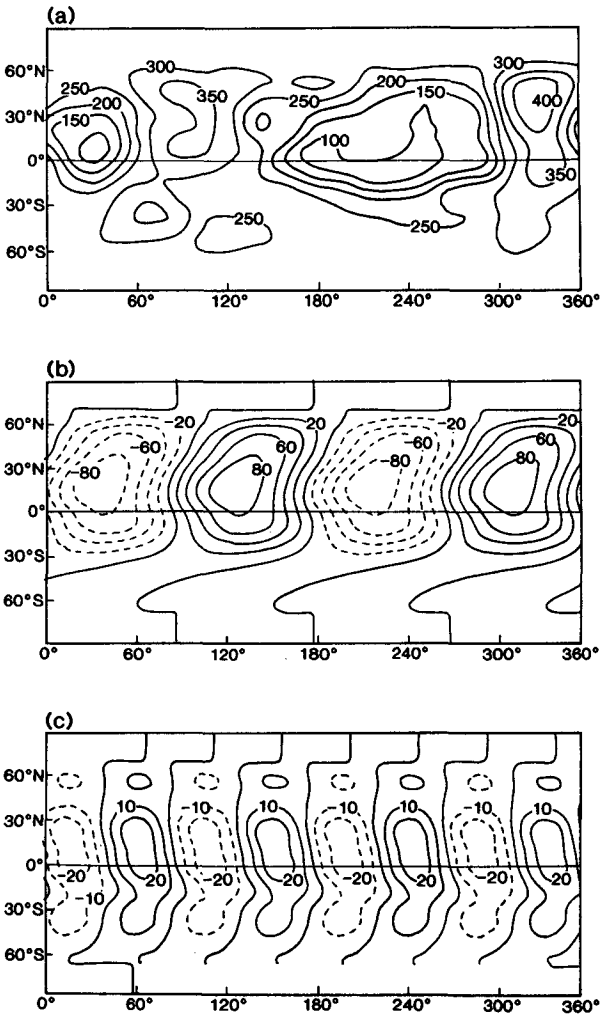

FIG. 4. (a) Surface thermal inertia distribution used in the GCM. Contour labels are in units of J m^{-2} $s^{-0.5}$ K^{-1}. (b) Zonal wavenumber 2 component of surface thermal inertia. (c) Zonal wave 4 component.

Heat and momentum exchange between the surface and the lowest atmospheric model layer is parameterized with a Monin–Obukhov surface drag formulation (Hicks 1976). A globally uniform surface roughness value of 16.62 cm was used. Just as for the air temperatures, the surface temperature is constrained to not fall below the critical temperature for CO_2 condensation. In addition, the surface albedo is adjusted to an "ice" value (0.60) when surface condensation is implied by the surface temperature and pressure (and returns instantly to the bare soil value once the surface temperature exceeds that for CO_2 condensation).

The topography was derived from the Digital Terrain Model of Mars (U.S. Geological Survey 1991). The original 1° × 1° data was first averaged to the 5° × 6° model grid. The topography was then smoothed by first truncating all heights above 10 km (flattening the tops of the highest volcanoes) and then Fourier filtering in longitude to retain only waves 0–6. The resulting model topography is shown in the top panel of Fig. 5. Important topographic features include the Tharsis highlands at 250° longitude and the Hellas Basin at 60° longitude. There is a significant upslope from the NH into the SH in the zonal mean. At most latitudes the topography is dominated by low zonal wavenumbers, notably a very prominent, nearly symmetric wavenumber 2 distribution. Figures 5b and 5c display the zonal

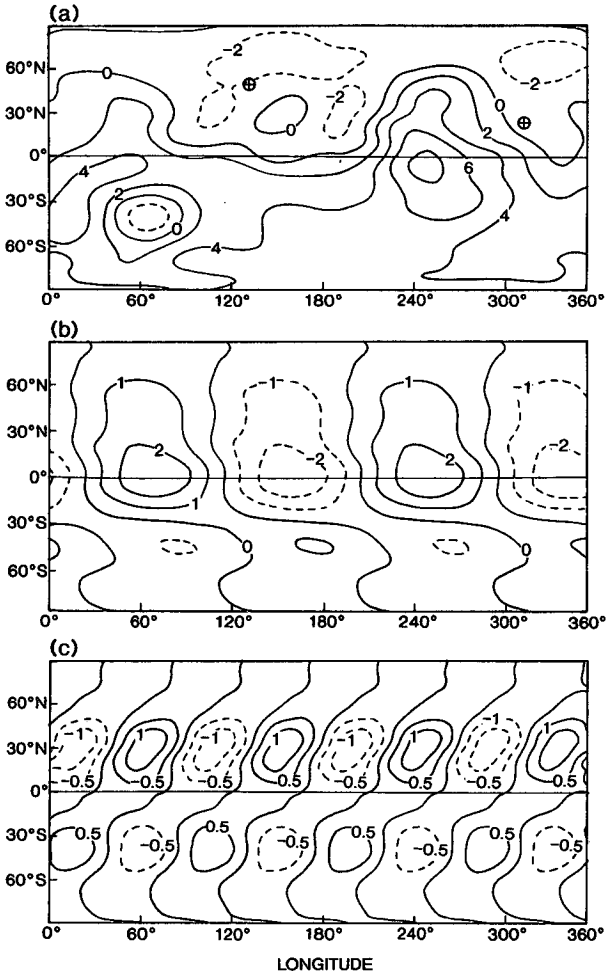

FIG. 5. (a) Topography used in the GCM. Contours are labeled in km and dashed contours denote negative heights. The zero level used is the same as in U.S. Geological Survey (1991), and the mean pressure in the model at zero height is about 6.1 mb. The locations of the two Viking lander sites are shown. (b) Zonal wavenumber 2 component of the topography. (c) Zonal wavenumber 4 component.

wavenumber 2 and 4 components of the present topography, respectively.

Several simulations will be discussed that were conducted at higher horizontal resolution (3° × 3.6°). These simulations employed the 5° × 6° resolution topography with the truncated volcanoes but without the zonal Fourier filtering. The thermal inertia and albedo fields for these experiments were interpolated versions of the filtered 5° × 6° resolution counterparts.

f. Transport of dust

While most of the experiments have been performed with prescribed dust concentrations, some integrations described at the end of section 6 involve a prognostic calculation of the dust mixing ratio. The resolved transport of tracer in these experiments is computed using a modification of the standard second-order box method to incorporate a fourth-order-accurate representation of the vertical advection term (Levy et al. 1982). The dust mixing ratio is also altered by the horizontal and subgrid-scale mixing parameterizations discussed earlier. In the simulations presented here, the aerosol is not mixed during convective adjustment. There is also an option to include a gravitational sedimentation. In these calculations, sedimentation was based on the Stokes–Cunningham relation appropriate for spherical particles with radius 2.5 μ (Conrath 1975).

5. Basic features of the model simulation

In this section the basic diurnally averaged features of the simulation obtained with the present GCM will be discussed. Observations of the latitude–height thermal structure are extremely limited (Zurek et al. 1992), and comparison is complicated by uncertainty in the aerosol distribution. For present purposes, comparisons will be made with the results of other GCMs that have been published, notably those from the NASA Ames model (Pollack et al. 1990; H93). One simplification in Martian modeling is the rather short time needed for the transient spin-up to a statistical equilibrium flow. Haberle et al. (1993a) investigated this issue in the NASA Ames GCM and found that the globally averaged kinetic energy in an integration from rest generally equilibrates in a time of the order of 20 sols. In practice, the present integrations typically begin with a 30 sol spinup period from rest or a 10–20 sol spinup from initialization from earlier fully developed integrations. In all cases, inspection of the time evolution of the mean state confirms that the zonal-mean flow has equilibrated by the end of the designated spinup period. Depending on the experiment, the analysis was performed over 10 or 20 sols following the initial spinup.

a. Zonal-mean temperature and winds

The simulated zonal-mean horizontal wind and temperature fields obtained in three experiments using aerosol optical depths τ of 0.3, 1.0, and 2.0 are displayed in Fig. 6. These results are for analysis periods centered on NH winter solstice (L_s = 270) and were obtained using the L16 model. Figures 2, 5, and 6 of H93 show comparable quantities obtained with the NASA Ames model. There is quite good overall agreement between the present simulations and those of H93. In particular, both the Ames model and the present model capture the strong meridional temperature gradient in the winter hemisphere with an associated intense westerly jet. The strength of this jet increases significantly with the optical depth employed. As dust loading is increased in the model, the atmosphere becomes warmer and the lapse rate becomes less steep. Features of the simulated winter hemisphere tempera-

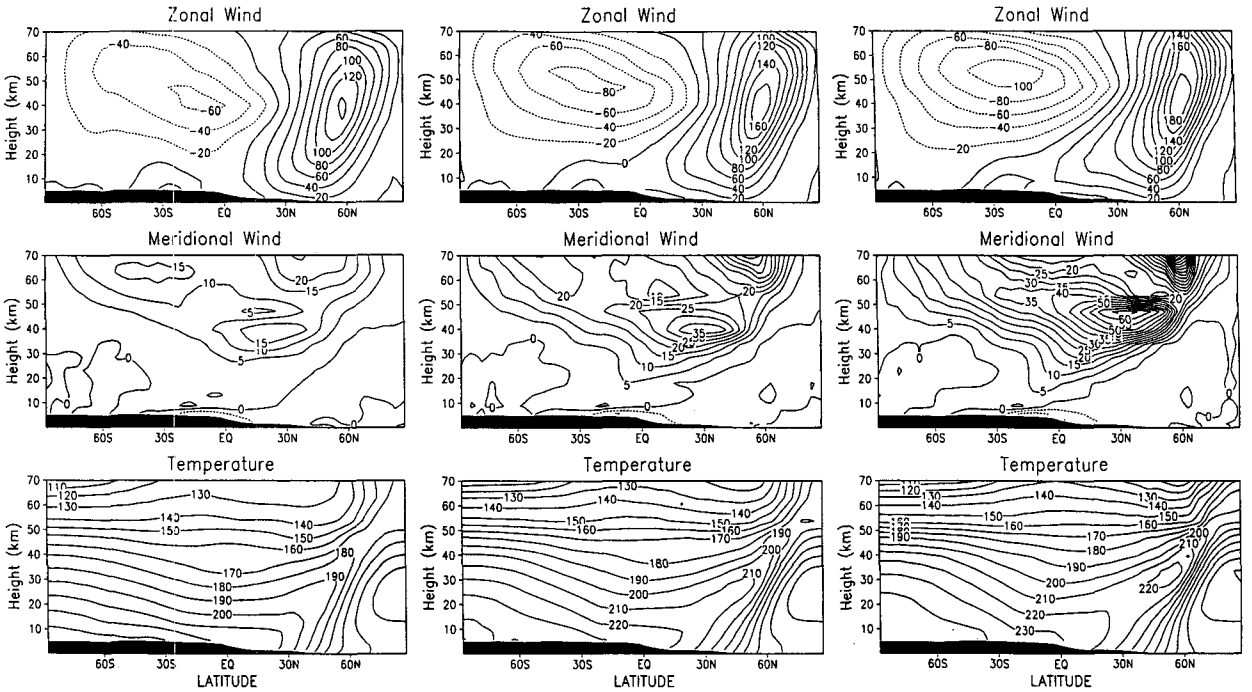

FIG. 6. Time-mean zonal-mean zonal wind, meridional wind, and temperature for NH winter (L_s = 270) integration with the 16-level version of the model. Results presented for three different dust concentrations corresponding to τ = 0.3 (left), τ = 1 (center), and τ = 2 (right). Wind contours labeled in meters per second; temperature contours are labeled in kelvin. Dashed contours denote westward and southward velocities for the zonal and meridional winds, respectively.

ture structure are in reasonable accord with IRIS observational results presented by Conrath (1981) for late NH winter (L_s = 346) using optical depths intermediate between 0.3 and 1.0.

The near-surface westerly jet in the summer hemisphere, seen in Fig. 6, is centered near the poleward extent of the lower branch of the cross-equatorial Hadley circulation. The strength of both the Hadley circulation and the low-level westerlies increase with optical depth. This behavior is also seen in the simulations of H93 and Hourdin et al. (1993). The increase in mass streamfunction with increasing optical depth is comparable to that seen in the Ames model. Perhaps the most notable difference between the Ames and GFDL model results is a somewhat stronger (by ~10 m s^{-1}) equatorial westerly flow at 10–30 km above the surface in the present model for higher aerosol loading.

There appears to be a tendency for the global mean in the present simulations to be slightly (~5–10 K) warmer than in the comparable Ames simulations. H93 compare temperatures from the Ames model with those of the Viking IRTM observations (centered at 0.5 mb or ~25 km) following the second 1977 dust storm (L_s ~ 280) and note that their model temperatures are too low at all latitudes, for all optical depths used. Thus, the present results appear to be in better agreement with observations. The differences in assumed vertical dust profiles and in the treatment of IR radiative transfer may both contribute to the discrepancy in global temperature between the two models. The present prescribed dust-mixing ratio is nearly constant up to 35 km, which is somewhat deeper than that used by H93. The omission of the aerosol emissivity in the 15-μ band in the present treatment of radiation could also account for some of the difference in global-mean temperature.

Of course, there are other sources of uncertainty in the treatment of the radiative properties of dust. For example, H93 speculated that the aerosol emissivity based on the Toon dust size spectrum is overestimated. The sensitivity of the present GCM results to the aerosol emissivity scheme was examined by conducting two additional simulations with visible optical depth, τ = 1.0. Each simulation used the same emissivity formulation but one employed twice the standard IR emissivity and one employed 0.5 of the standard IR emissivity. Temperatures in the simulation with reduced emissivity exceed those in the increased emissivity experiment by about 12 K throughout the Tropics. The Hadley cell circulation is intensified in the increased emissivity case and the summer hemisphere subtropical jet strengthens. Zonal-mean winds elsewhere below 40 km show virtually no difference between the two experiments, however. Tidal surface pressure amplitudes are roughly 25% larger in the increased emissivity experiment relative to those in the reduced emissivity case.

The CO_2 IR scheme proposed by Hourdin (1992) was implemented to examine model sensitivity to this aspect of the radiation formulation. A comparison of GCM simulations employing the two CO_2 IR schemes indicates that model zonal mean temperatures are somewhat warmer (~4 K) with the Hourdin scheme, consistent with the weaker predicted cooling. This difference decreases with increased aerosol heating. Zonal-mean winds and tides are quite insensitive to the differences in the two formulations.

During NH summer ($L_s = 90$), the simulated Martian temperature field is similar (mirror image) to that for NH winter but is about 10 K cooler at low altitudes in the Tropics (for $\tau = 0.3$). The strength of the SH winter hemisphere jet is comparable to its NH winter counterpart, but the near-surface summer hemisphere subtropical westerly jet is considerably weaker for NH summer than for SH summer. As with the Ames model, the mass transport streamfunction is roughly half the value obtained during NH winter for comparable dust loading. This weaker circulation is associated with the reduced solar insolation at this time of year (close to aphelion). Simulations with an axisymmetric version of the model indicate that the zonal-mean topographic slope between the two hemispheres strongly inhibits the strength of the Hadley circulation during NH summer solstice.

Simulations were also carried out for near-equinoctial conditions ($L_s = 180, \tau = 0.3, 1.0, 2.0$). The model zonal-mean circulation in these cases is rather symmetrical between hemispheres, with relatively broad westerly jets in both hemispheres having peak winds of approximately 80 m s^{-1} at 60° lat. The midlatitude temperature profiles are less statically stable than those in the winter hemisphere at the solstices. In the equinoctial simulations there are equatorial zonal-mean westerlies at roughly 10–30 km in height. These equatorial westerlies become stronger with increased optical depth. As in the case of the NH winter solstice simulations discussed earlier, the present model near equinox produces stronger equatorial westerlies in this height range than does the Ames model (~10 m s^{-1} bias for $\tau = 0.3$).

It is well known that the presence of mean westerlies (i.e., atmospheric superrotation) on the equator must result from eddy momentum transports. One possibility is that the momentum flux divergence associated with the diurnal tide might generate the equatorial westerlies. In fact, the classical tidal theory calculations of Hamilton (1982) and Zurek (1986) suggest that the diurnal tide should provide a westerly driving of the equatorial mean flow in the lowest ~30 km of the Martian atmosphere (i.e., in the region of radiative tidal excitation). To examine this possibility, the present equinoctial simulations were repeated for a version of the GCM employing diurnally averaged solar radiation. In this simulation the equatorial westerlies are no longer present, confirming that the tides are contributing significantly to the atmospheric superrotation.

Many of the L16 model simulations were also repeated with the 40-level version of the model. These simulations compare extremely well with the L16 model in the lower atmosphere (up to 30 km) for all seasons. The most notable differences occur at high latitudes and altitudes in the NH near winter solstice and are apparently a result of the higher top boundary and different vertical distribution of imposed Rayleigh drag. One striking aspect of Fig. 6 is the increasingly strong meridional circulation at higher dust loadings and the resultant warming (due to the associated adiabatic heating) above 40 km in the winter polar region. This high-altitude winter pole warming is related to the closing off of the winter zonal jet by thermal wind balance. This behavior is more pronounced in the L40 version of the model than the L16 version. The meridional jet is part of a pole-to-pole circulation similar to but much stronger than that in the terrestrial mesosphere (e.g., Andrews et al. 1987). Associated with the meridional circulation are very strong equatorial easterlies giving a very pronounced semiannual oscillation. When the model is run without any Rayleigh damping, these easterlies can approach the solid body rotation velocity of 240 m s^{-1} at the equator. Interestingly, there is some limited evidence from ground-based observations (Lellouch et al. 1991) for very strong (~160 ± 80 m s^{-1}) equatorial easterlies in the Martian upper atmosphere between 50 and 80 km. The simulated circulation appears to have the character of a strongly nonlinear Hadley circulation as discussed by Dunkerton (1989, 1991). The strength of the meridional circulation increases as the depth of the domain (and thermal forcing) increases. As noted earlier in section 4, the imposition of Rayleigh friction in this model has the effect of limiting the strength of the meridional circulation, particularly in the NH winter simulations. This circulation is independent of effects of the rigid lid at the upper boundary. For the more weakly forced circulation of NH summer, there is considerably less difference in simulations with and without the Rayleigh damping. It is evident that much work remains in specifying the character and distribution of drag in the middle atmosphere.

b. Stationary and baroclinic waves

Maps of the simulated wind, temperature, and geopotential averaged over the 10–20 sol analysis periods reveal the presence of strong stationary eddies, particularly in the winter hemisphere [where westerly mean flow should permit substantial vertical wave propagation of zero-frequency linear Rossby waves, e.g., Charney and Drazin (1961)]. Zonal wavenumber 2 is especially prominent in the NH winter, while wavenumber 1 dominates in the SH winter. Conrath (1981) found observational evidence of wavelike temperature

perturbations in northern midlatitudes during late NH winter which may be interpreted as an indication of a wavenumber 2 stationary eddy. Stationary waves are also prominent in the simulations at tropical latitudes. These features appear to be primarily the result of thermal forcing associated with the highlands that act as elevated heat sources as was anticipated by Webster (1977). For example, a thermally direct longitudinal circulation is associated with the stationary zonal wave 2 feature in the zonal wind field. It will be shown later that this circulation has significance for aerosol transport. An interesting feature of the present model is the appearance of a prominent zonal wave-3 stationary wave in the meridional velocity at equatorial latitudes in the high dust simulations. Latitude–height sections (not shown) reveal a band of strong eddy wave amplitude extending from near the surface in the latitudes of the SH subtropical westerly jet upward and northward through the equatorial westerlies into the Northern (winter) Hemisphere. Examination of simulations with different dust loadings indicates that the penetration of such waves into the Tropics is enhanced by stronger equatorial zonal mean westerlies. As noted earlier, the strength of the equatorial westerlies is one area of significant disagreement between the present model and the Ames model. It would be interesting to see if there is a consistent difference in the low-latitude stationary wave field in the two models.

Transient baroclinic wave activity is clearly seen in the simulated model surface pressure field. In NH winter, such activity is particularly prominent near the latitude of VL2 (48°N) and is characterized by very coherent eastward propagating waves with zonal wavenumbers 1–5 and periods of 2–10 days, consistent with values deduced from Viking data (Barnes 1980, 1981). The model surface pressure fluctuations at the VL2 site have typical amplitudes ~0.25 mb, which is quite similar to that observed. The simulated oscillations tend to be somewhat more regular than those observed by VL2, however. In particular, from midwinter into spring, zonal wavenumber 3 with a period of roughly 2.2 days is especially prominent. The simulated baroclinic waves at VL1 (22°N) are generally ~0.03 mb, which is a factor of ~2 weaker than observed at VL1 during the first Viking year. Interestingly, during the NH winter of the third Viking year, the pressure oscillations at VL1 were observed to be markedly stronger than earlier in the mission (VL2 measurements were not available for this period). The VL1 transient pressure fluctuations in the present simulations are much smaller (factor of ~4) than those observed in the third year. Baroclinic activity is considerably weaker in the SH winter simulation than in the NH winter, a feature also seen in the Ames GCM (Barnes et al. 1993).

c. *Diurnally averaged surface wind*

Figure 7 shows the GFDL L40 model simulation of near-surface (~100 m) wind fields, averaged over 20 days, for NH winter ($L_s = 270$, $\tau = 1.0$) and NH summer ($L_s = 90$, $\tau = 0.3$). A similar figure for NH winter is given in Hourdin et al. (1993). The trade-wind pattern of the surface branch of the cross-equatorial Hadley cell circulation is clearly evident in both seasons. There is also considerable topographic influence on the surface winds. The near-surface winds at VL1 change from northerly in summer to southerly in winter as observed. Significantly, the winds at VL2 during NH winter solstice change from westerly to northeasterly as the dust loading τ is increased (from 0.3 to 1). A similar shift was observed following the 1977b global dust storm.

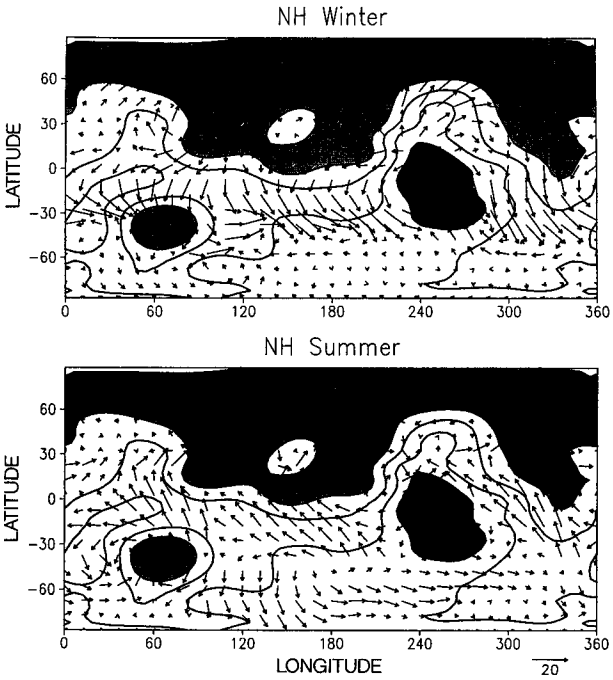

FIG. 7. The time-mean winds at the lowest model level (~100 m above the surface) in a NH winter simulation with $\tau = 1$ (top) and for a NH summer simulation with $\tau = 0.3$ (bottom). The arrow at the lower right represents 20 m s^{-1}. Also shown is the model topography with 2-km contour intervals. Light shading denotes topographic elevations below zero, while dark shading denotes areas more than 6 km above zero.

A longitude–height section of the meridional winds along the equator is shown in Fig. 8. The low-level winds (~5 km deep) of the Hadley circulation are much stronger for the NH winter solstice case than for the summer solstice case. Joshi et al. (1994, 1995) have proposed that Martian winds are influenced by a western boundary current effect similar to that postulated to explain the low-level Somali jet along the eastern edge of the East Africa highlands. Figure 8 clearly shows intensification of the meridional wind along the eastern flanks of topographic highlands in the NH summer case. The boundary current effect and the subtropical zonal jet associated with the Hadley circulation to-

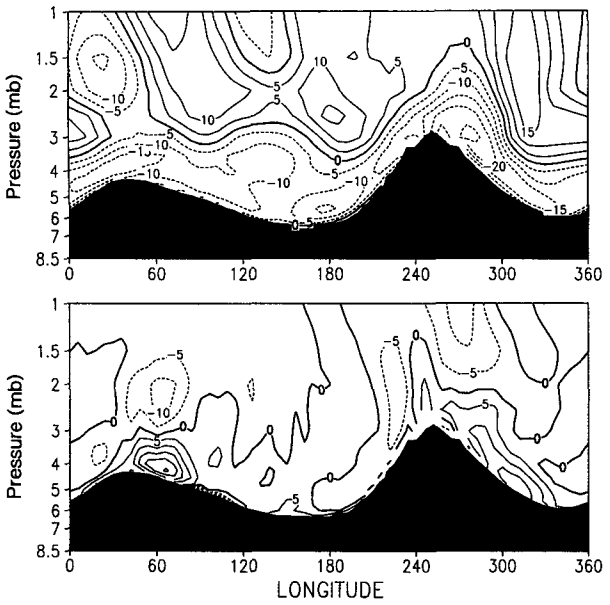

FIG. 8. A longitude-height plot of the time-mean meridional winds along the equator for the two simulations in Fig. 7. NH winter, $\tau = 1$ (top) and NH summer, $\tau = 0.3$ (bottom). The vertical coordinate is pressure in mb. Contours are labeled in m s^{-1}, and dashed contours denote southward velocities.

gether suggest a strong similarity with the summer Indian monsoon circulation. The distribution of the meridional wind in the Tropics for the NH winter case shows the zonal wave 3 stationary wave at higher levels.

6. Results for the tidal fields

In this section the results for the diurnal and semidiurnal harmonics of the simulated Martian atmospheric fields will be considered. The main focus will be on the surface fields for which there are some comparable observations. Each of the individual experiments described here consists of a spinup period (starting from rest or from another experiment) of typically 15–30 sols, followed by a 10–20 sol period in which hourly (24 "hours" per sol) data are analyzed to determine the diurnal cycle. The annual march of solar zenith angle is included in all of these rather short experiments, each of which will be labeled by the areocentric longitude at the middle of the integration.

a. Simulated surface pressure oscillation and effects of lower-boundary modifications

Figure 9 shows the spatial distribution of the diurnal and semidiurnal surface pressure amplitudes for NH summer ($L_s = 90$) experiment with $\tau = 0.3$ and the full geographical distribution of topography, surface albedo, and surface thermal inertia. The amplitude is normalized by the local time-mean pressure. There is a striking zonal wavenumber-2 modulation in the diurnal surface pressure response with maximum amplitudes over lowlands. There is an even more marked wavenumber-4 modulation of the semidiurnal tide response. The local time phases (not shown) of $S_1(p)$ and $S_2(p)$ also display the prominent wavenumber 2 and wavenumber 4 modulations, respectively. The strong variations in phase and amplitude of $S_2(p)$, even at low latitudes, contrasts markedly with the observations of the semidiurnal tide in the terrestrial atmosphere (e.g., Chapman and Lindzen 1970). The basic pattern of zonal modulation seen in this figure is apparent as well in the unnormalized $S_1(p)$ amplitudes.

The zonal wave-2 geographical pattern seen in the (local time) diurnal tide is just what is expected to result from the interference of eastward and westward wave 1 components. Similarly, the wave-4 pattern in the semidiurnal tide is consistent with the interference of eastward- and westward propagating wave 2 components. The diurnal and semidiurnal pressure signals in the model simulation have been decomposed into eastward and westward propagating zonal wavenumber-1 and wavenumber-2 modes respectively; that is,

$$\begin{aligned} S(p) = {} & A_{11}\cos(\phi + 2\pi t - \delta_{11}) \\ & + A_{1-1}\cos(\phi - 2\pi t - \delta_{1-1}) \\ & + A_{22}\cos(2\phi + 4\pi t - \delta_{22}) \\ & + A_{2-2}\cos(2\phi - 4\pi t - \delta_{2-2}) \\ & + \text{other components}, \end{aligned}$$

where ϕ is the east longitude, t is the universal time (UT) in sols, and the amplitudes and phases are functions only of the latitude. The amplitudes and phases for the four components isolated are shown in Fig. 10. The eastward diurnal and semidiurnal components seen in Fig. 10 do display the equatorial trapping and minimal meridional phase propagation expected for Kelvin modes. The narrower equatorial confinement for A_{2-2} than for A_{1-1} is also consistent with the linear theory of the Kelvin mode. The phase angles δ_{11} and δ_{22} also define a local time of maximum pressure for the sun-synchronous tides. For example, the value of 280° obtained for δ_{22} over the Tropics and subtropics corresponds to the sun-synchronous component of $S_2(p)$ peaking near 0920. This is slightly later than predicted by the classical theory. The diurnal phases are in rough agreement with classical tidal theory.

To demonstrate the significance of the wavenumber 2 boundary forcing, a simulation was conducted with the boundary modified by the removal of the zonal wave-2 topographic component and by the imposition of globally uniform surface thermal inertia and albedo. The resulting amplitudes for $S_1(p)$ and $S_2(p)$ are shown in Fig. 11. The result for $S_1(p)$ is much more zonally uniform than in the standard experiment, revealing the virtual absence of the eastward propagating

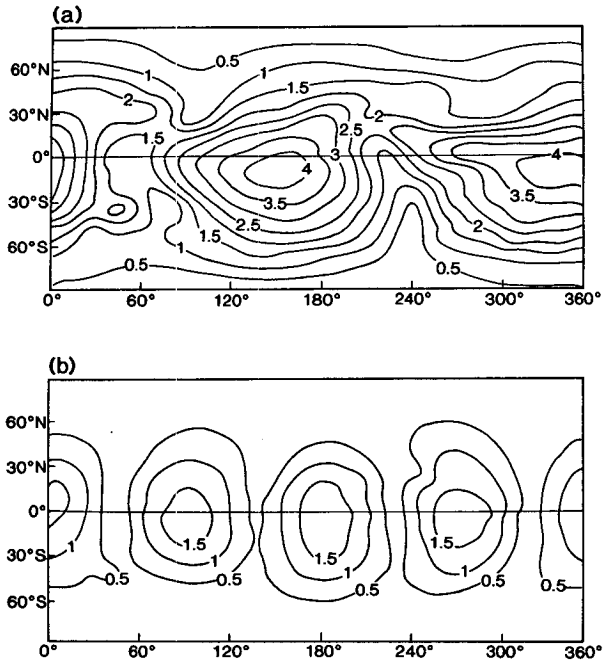

FIG. 9. (a) Amplitude of $S_1(p)$ normalized by the time mean local pressure from a NH summer (L_s = 90) model experiment using realistic topography and surface thermal inertia, and with a uniform dust distribution with τ = 0.3. Contour labels are in percent. (b) As in (a) but for the amplitude of $S_2(p)$.

diurnal Kelvin mode. There are still strong zonal variations in $S_2(p)$ in the modified topography case, but the phase of the semidiurnal interference pattern is shifted westward relative to the standard case. Figure 12a presents the equatorial values of the phase (local time of pressure maximum) for $S_1(p)$ in both the full and modified topography experiments. In the full topography case, this local phase advances toward the west, suggesting that $S_1(p)$ is dominated by eastward propagating wave 1. By contrast, in the modified topography case, the local phase of $S_1(p)$ is quite constant, consistent with the view that $S_1(p)$ is dominated by the sun-synchronous component. The phase of $S_2(p)$ for the same integration is shown in Fig. 12b, also indicating a wave 4 longitudinal modulation and the westward shift in phase pattern when wave 2 boundary forcing is removed.

A set of three experiments was carried out to examine the individual contributions of variable topography, surface thermal inertia, and surface albedo to the diurnal Kelvin mode excitation. In a simulation with realistic topography and geographically uniform surface thermal inertia and albedo, the diurnal Kelvin mode has a peak amplitude A_{1-1} of 165 μbar with corresponding δ_{1-1} of 190°. A simulation using the observed surface thermal inertia, uniform albedo, and no topography produced a diurnal Kelvin mode with a maximum amplitude A_{1-1} of 95 μbar and a phase δ_{1-1} of 300°. The integration with the observed geographical variation of surface albedo, but no topography or variations in surface thermal inertia, yielded a much weaker Kelvin wave (maximum amplitude A_{1-1} = 10 μbar). A comparison with Fig. 10 (A_{1-1} of 150 μbar and δ_{1-1} of 220°) suggests that the total diurnal Kelvin wave response is at least roughly consistent with the linear superposition of the effects of realistic topography and surface thermal inertia.

b. *Idealized calculations*

The results discussed in section 6a confirm the simple picture in which both the diurnal and semidiurnal tides are dominated by the sum of the sun-synchronous component and a component propagating with the same phase speed toward the east. The interference of these components leads to very pronounced geographical variability in the tide as seen at the surface.

To explore further the excitation of these eastward-propagating tidal components, a number of experiments were conducted with the L16 version of the model using idealized distributions of topography and surface thermal inertia. In all these experiments the surface albedo was globally uniform. One version had no topography and a surface thermal inertia given by

$$I(\theta, \phi) = \mathcal{A}_I[1.25-0.75\cos(2\phi)],$$

where $\mathcal{A}_I$ is the amplitude (taken to be 200 J m^{-2} s$^{-0.5}$ K^{-1}), while the other had uniform surface thermal inertia and topographic heights given by

$$Z(\theta, \phi) = \mathcal{A}_Z\cos\theta\cos(2\phi),$$

where $\mathcal{A}_Z$ is the topographic amplitude and θ is latitude. Note that when $\mathcal{A}_Z \sim 2$ km, the idealized topography very roughly resembles the wave-2 component of the full topography (see Fig. 5b). The phases of these idealized distributions are chosen so that the longitudes of the topographic peaks correspond to the minima in the surface thermal inertia. In all cases, the model was spun up from rest for 15 days and diurnal composite fields were constructed from the subsequent 15 days. The zonal-mean fields for these experiments will not be shown, but in general these results do not differ substantially from those discussed earlier for the full model (section 5).

1) KELVIN NORMAL MODE RESONANCE

A set of experiments was conducted with the purpose of determining the behavior of the amplitude of the diurnal and semidiurnal Kelvin wave response to variations in the mean temperature of the atmosphere. In each integration, a prescribed globally uniform offset was introduced to the temperature used in the dynamics code only, but not in the radiation, soil model, or convective adjustment routines. This allowed the model dynamics to respond to the imposed temperature

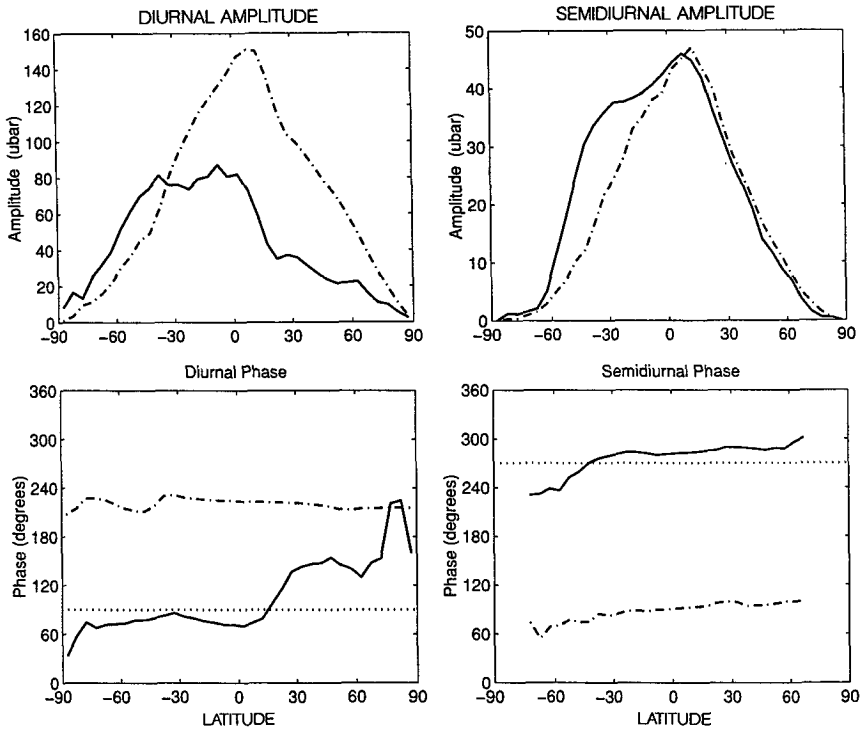

FIG. 10. Results of the decomposition of $S_1(p)$ and $S_2(p)$ into westward-propagating (solid) and eastward-propagating (broken) waves 1 and 2, respectively, for the experiment described in the caption to Fig. 9. Phases are in degrees longitude at 0 universal time (see text). Dashed lines in the phase plots represent equivalent phases of 0600 and 0900 hours for the westward (sun-synchronous) diurnal and semidiurnal tides, respectively.

change, while leaving the thermal forcing of the tides essentially identical for each simulation. In fact, the zonal-mean zonal wind and temperature fields (apart from the offset) showed virtually no change over the range of offset temperatures employed, at least below ~40 km. Several series of simulations were carried out for different seasons and optical depths. The first series examined the resonant response for NH winter (L_s = 270, τ = 0.3) using $\mathcal{A}_Z$ = 2.0 km. Figure 13 displays the maximum amplitudes and equatorial phases of the diurnal and semidiurnal eastward propagating components as a function of the imposed temperature perturbation. Zero temperature offset corresponds to the standard model atmospheric state for this season. There is a clear signature of resonance in the peaked amplitude structure and monotonic ~180° change in phase of the diurnal Kelvin wave as the temperature increases. The standard model, in this season, has an atmosphere that is warmer by ~28 K than that at the resonant peak. The phase behavior indicates an increasing westerly lag in the response to eastward propagating forcing as the mean temperature decreases. The phase angle of −25° at the resonant peak corresponds to a 0000 UT pressure maximum 12.5° west of the topographic maximum at 0° long. Even in the simple classical theory case, the Kelvin modes on the sphere are slightly dispersive (Longuet-Higgins 1968). This is consistent with the behavior of Fig. 13 where the semidiurnal Kelvin mode is seen to peak at slightly warmer mean temperatures than the diurnal mode. Also shown in Fig. 13 is the maximum amplitude of the eastward wave 3 component of $S_3(p)$. This also has a distinct resonance peak with the maximum displaced slightly from that of the semidiurnal resonance. In strong contrast to the behavior of the eastward propagating waves, the sun-synchronous components of $S_1(p)$ and $S_2(p)$ display only a very moderate increase in amplitude as the mean temperature is reduced over the range shown.

Additional resonance series integrations were performed for τ = 0.3 near equinox (L_s = 0) and in NH summer (L_s = 90), and for τ = 1.0 in NH winter (L_s = 270). The results for the maximum amplitudes are summarized in Fig. 14. There is a resonant peak in each case, with the maximum amplitude increasing with the strength of thermal forcing (note that the solar insolation at L_s = 270 is about 40% larger than at L_s = 90). Of course, with increased solar flux, the atmosphere is warmer in the global mean, and so a larger temperature offset is required for resonance. In all cases, the 0 K temperature offset appears to be on the subresonant wing of the response curves, with the coldest of the simulated states (L_s = 90, τ = 0.3) being most nearly

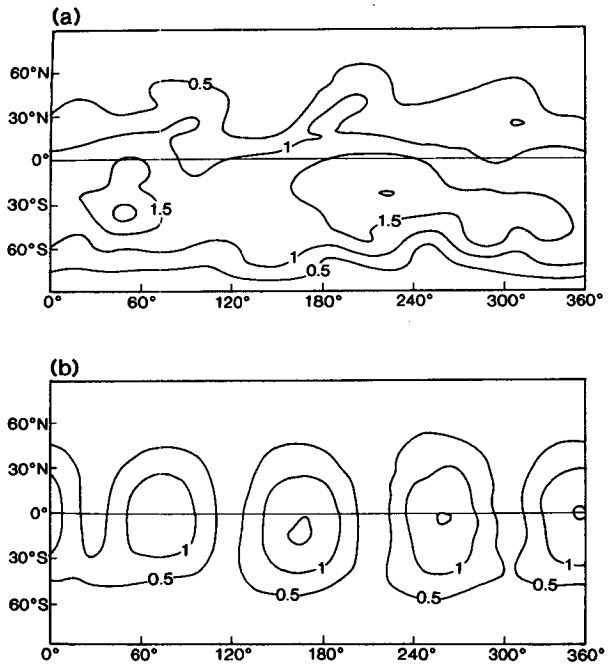

FIG. 11. As in Fig. 9 but for an experiment in which the model had been modified by the removal of the zonal wavenumber 2 component of topography as well as all inhomogeneities in surface thermal inertia and surface albedo.

resonant. This is in agreement with Zurek's (1988) conclusion that the diurnal Kelvin wave would be most nearly resonant during the relatively cooler NH summer season.

The half-width of the resonance curves in Figs. 13 and 14 was examined in the context of classical tidal theory with thermal damping. Solutions to the vertical structure equation appropriate for the diurnal Kelvin mode were obtained for a range of temperature offsets applied to a vertical profile based on the GCM temperatures. Damping was incorporated as a vertically uniform Newtonian cooling. A comparison of these simple calculations (not shown) with the GCM results for the Kelvin mode in Figs. 13 and 14 suggests that, in the full model, the net effect of all the damping mechanisms for the Kelvin wave is equivalent to an effective Newtonian cooling timescale of the order of 0.5–1.0 days. This relatively strong effective damping allows the Kelvin wave to equilibrate fairly rapidly (within 15 days) in these experiments. By contrast, the sun-synchronous components largely achieve their final amplitudes within 2 days, even as the zonal flow continues to adjust.

2) DEPENDENCE OF KELVIN MODES ON THE AMPLITUDE OF TOPOGRAPHY

Additional experiments have been conducted to examine the influence of the amplitude of the topographic variation in determining the Kelvin wave response. Three sets of experiments, all with $\tau = 0.3$, and corresponding to NH winter ($L_s = 270$), equinox ($L_s = 0$), and NH summer ($L_s = 90$) were performed. Each set consisted of six individual experiments, all identical except for the amplitude of the wave 2 topography employed. Although $\mathcal{A}_Z$ varied over a range from 0.5 to 5 km in each series, the zonal-mean circulation below 40 km showed little change among the different experiments in each set. At higher altitudes, the strength of the equatorial easterlies was decreased with increasing topographic amplitude. The sun-synchronous components of $S_1(p)$ and $S_2(p)$ also showed little dependence on topographic amplitude. The maximum amplitude of the eastward propagating wave-1 component of $S_1(p)$ for each experiment is plotted as a function of $\mathcal{A}_Z$ in Fig. 15a. For given L_s, the diurnal Kelvin wave response can be seen to vary almost linearly with the amplitude of the imposed topography. A comparison with the diurnal Kelvin wave from the realistic topography-only experiment (165 μbar) suggests an effective topographic amplitude between 1 and 2 km. Also shown in Fig. 15b is the comparable measure of the amplitude of the semidiurnal wave 2 Kelvin wave plotted as a function of the diurnal Kelvin wave amplitude for each of the experiments. The amplitude of the semidiurnal Kelvin wave appears to have a quadratic dependence on the diurnal Kelvin wave strength, at least at the smallest wave amplitudes. This is an indication of the nonlinear nature of the excitation for the semi-

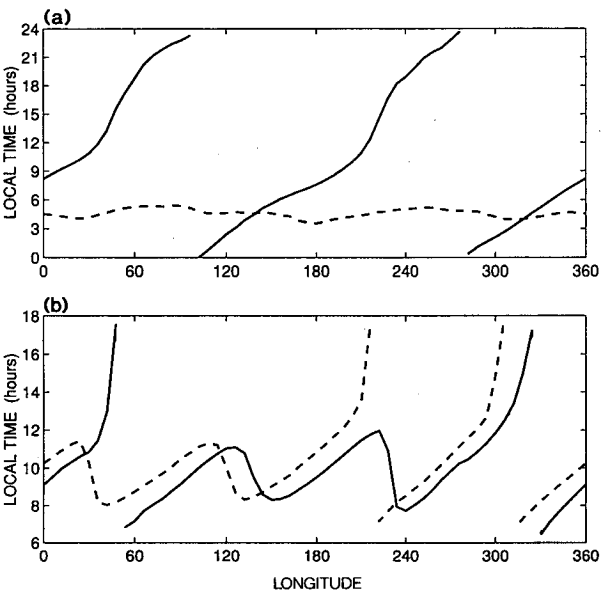

FIG. 12. (a) The equatorial local time phase of $S_1(p)$ for the simulation with realistic boundary conditions (solid line, corresponding to Fig. 9), and the experiment with modified lower boundary conditions (dashed line, corresponding to Fig. 11). (b) As in (a) but for $S_2(p)$.

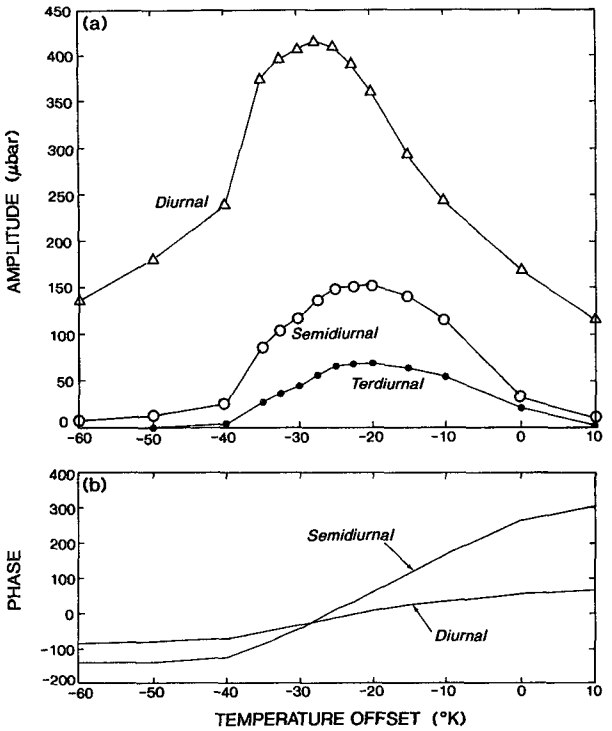

FIG. 13. (a) Maximum amplitude of the eastward propagating wave-1 component of $S_1(p)$, the eastward propagating wave-2 component of $S_2(p)$, and the eastward-propagating wave-3 component of $S_3(p)$. All are plotted as a function of the uniform temperature offset imposed in individual experiments. These integrations were conducted with the 16-level version of the model for NH winter (L_s = 270) conditions with τ = 0.3 with idealized topography. (b) The phases of the eastward propagating wave-1 component of $S_1(p)$ and of the eastward propagating wave 2 component of $S_2(p)$. The phase in each case is determined at the latitude of maximum amplitude.

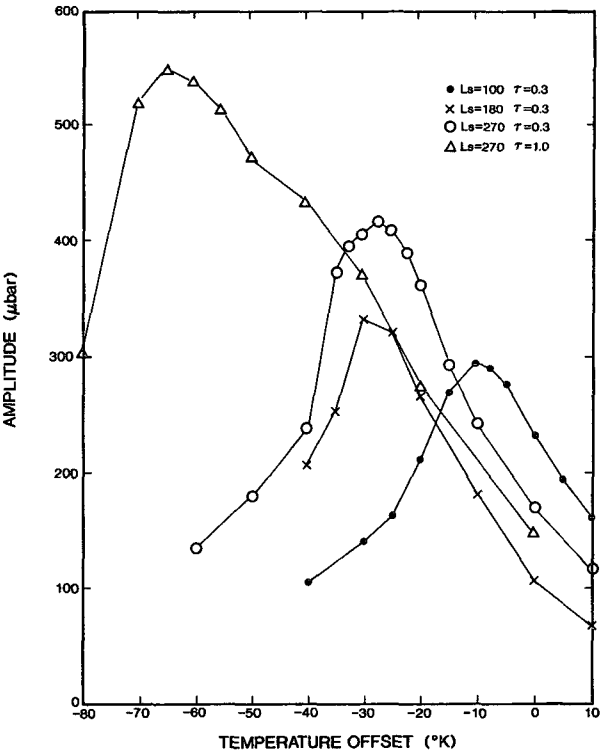

FIG. 14. The maximum amplitude of the eastward propagating wave-1 component of $S_1(p)$ plotted as a function of the imposed temperature offset for four cases: NH summer (L_s = 90) with τ = 0.3, equinox (L_s = 0) with τ = 0.3, NH winter (L_s = 270) with τ = 0.3, and NH winter (L_s = 270) with τ = 1. All cases employ idealized topography with 2-km amplitude.

diurnal Kelvin mode. It is interesting that under realistic conditions ($\mathcal{A}_Z \sim 2$ km), the amplitude of the semidiurnal Kelvin wave can be a substantial fraction of that of the diurnal Kelvin wave, even in this case with no direct boundary forcing of the semidiurnal wave. The composite march of surface pressure through the day due to the eastward propagating waves was computed (not shown). The nonlinear interaction that generates the semidiurnal component (and higher harmonics) appears as a steepening of the eastward propagating waveform. The results in Fig. 15 suggest that the nonlinear generation of the semidiurnal Kelvin wave does begin to saturate once the Kelvin wave amplitude exceeds about 300 μb.

3) ROLES OF TOPOGRAPHY AND THERMAL INERTIA INHOMOGENEITY IN EXCITING THE KELVIN NORMAL MODE

The effect of the zonal variations in surface thermal inertia in modifying the sun-synchronous forcing for the tides is easy to understand. Over locations with

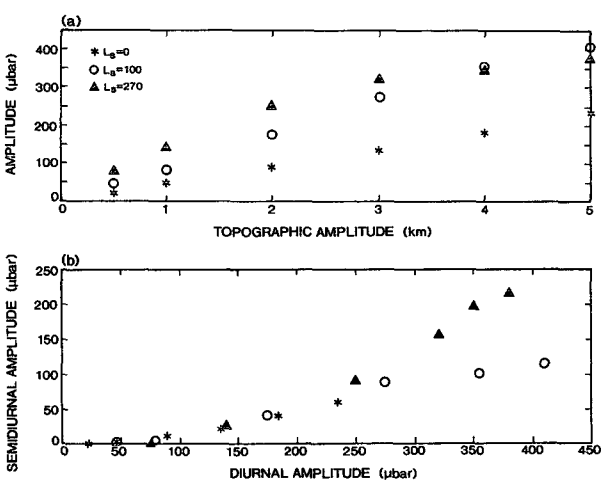

FIG. 15. (a) Diurnal Kelvin wave amplitude in the idealized topography case plotted as a function of the topographic height. Triangles represent NH summer, open circles for NH winter, and stars for equinox (L_s = 0). The optical depth in all three cases is 0.3. (b) Semidiurnal Kelvin wave amplitude plotted against the diurnal Kelvin wave amplitude for the idealized topography simulations.

small surface thermal inertia, the daily variation of surface temperature is large, leading to enhanced heating of the overlying atmosphere due to convection and upward IR flux. This effect produces a distortion of the diurnal (and harmonics of the diurnal) atmospheric heating, which depends on the geographical distribution of the surface thermal inertia. As noted earlier, the zonal wave 2 component of such a distortion of the sun-synchronous heating will force the near-resonant diurnal wave 1 Kelvin mode.

The influence of topography is potentially more complicated. One obvious effect is simply to elevate the sources of convective heating (and atmospheric heating due to upward IR from the surface) over highlands. From classical tidal theory it is apparent that the same total heating (in W m^{-2}) is more effective at forcing tides when it is concentrated at higher levels (e.g., Chapman and Lindzen 1970). It is more difficult to predict what effect the dynamical modifications (Zurek 1976) induced by topography should have on the tidal fields.

The present study included a calculation employing the idealized distribution of surface thermal inertia described in section 6b.1 in the absence of topography. This experiment was performed for NH winter conditions and $\tau = 0.3$. An eastward wave 1 diurnal Kelvin wave is excited, with an amplitude about 40% of that in the 2-km topography case. The phase of the surface thermal inertia minima is such that the eastward propagating component of heating has a maximum at 180° long at 0000 UT (as does the sun-synchronous heating). As the atmosphere passes through resonance (warm atmosphere to cool), the resulting Kelvin wave phase δ_{1-1} increasingly lags that of the forcing, changing from 270° through 180° to 90° as classical tidal theory predicts. It is evident from Fig. 13 that this behavior is nearly 180° out of phase with that of the comparable idealized topography experiment (note that the phases of the idealized distributions described in 6b.1 are chosen so that the modulated thermal heating effects should be equivalent). Evidently the dynamical influences of topography oppose and overwhelm the "thermal" effect. Dynamical contributions to Kelvin wave forcing include divergence effects due to tide-induced slope winds and mean mass advection.

In his theoretical study, Zurek (1976) concluded that Kelvin wave excitation would be strongly dependent on the near-surface static stability. No evidence of such a strong dependence was seen in the present study. Of course, in these nonlinear simulations, there is a strongly stable boundary layer over the nighttime longitudes so that the idealization of a zonally uniform near-adiabatic ambient temperature is never even approximately realized. The Kelvin wave amplitudes obtained in this study are considerably smaller than those predicted by Zurek for clear-sky conditions. This may be due to limitations in Zurek's truncated solution in his formulation of the tidal dynamics, or to the presence of much larger effective damping in the GCM simulations, or that a zonal-mean near-adiabatic lapse rate is not obtained.

The analysis of the "thermal" and "dynamical" consequences of the topography is complicated by the distortion of the dust distribution by the topography. In the present formulation [Eq. (4.1)], there is a larger total column of dust above lowlands than highlands, which tends to counteract the elevated heating effect. In a simulation with atmospheric aerosol expressed as function of the terrain-following sigma coordinate rather than pressure, the Kelvin wave amplitude is decreased while the phase remains the same. In the idealized calculations discussed here, the Kelvin wave at resonance has roughly the same phase, even without dust ($\tau = 0$). The forcing due to the modulation of the dust distribution by topography evidently acts nearly in phase with the dynamical topographic effect.

These results have interesting implications for the tides in simulations with realistic geographical distributions of topography and surface thermal inertia. The phases of the Kelvin wave corresponding to the realistic topography and surface thermal inertia, each regarded separately, are consistent with the results from the idealized calculations. Comparison of Figs. 4 and 5 show that there is a very rough correlation between high topography and low surface thermal inertia. This means that the excitation of the Kelvin wave can be considered as a sum of two terms of roughly opposing phases.

4) VERTICAL STRUCTURE OF THE TIDAL FIELDS

Figure 16 shows latitude–height plots of the sun-synchronous diurnal tidal fields for a NH winter solstice simulation with $\tau = 0.3$, $\mathcal{A}_Z = 2$ km, and uniform surface thermal inertia. The vertical extent is roughly 60 km, corresponding to the bottom 32 levels of a 40-level simulation. The amplitudes of the diurnal harmonics of temperature, zonal, and meridional wind [$S_1(T)$, $S_1(u)$ and $S_1(v)$, respectively], and the phase of $S_1(u)$ are all presented. The harmonic analysis was performed using data on the model coordinate surfaces and the results are plotted as functions of the corresponding pressure for a standard atmosphere. The most striking aspect of the $S_1(T)$ amplitude is the strong surface maximum near the subsolar latitude. The maximum amplitude at the lowest model level ($\sim$100 m) is 23 K, corresponding to a diurnal temperature range of 46 K, which may be compared to the simulated range of surface temperature, which exceeds 80 K at the subsolar latitude. Above about 20 km, the $S_1(T)$ amplitude has three distinct peaks, one in low latitudes that tilts into the winter hemisphere with height, one near 50°N, and one near 50°S. In the extratropics, the phase (not shown) is roughly constant (with temperature perturbation peaking near 1800 local time), while the low-latitude phase displays a vertical propagation with

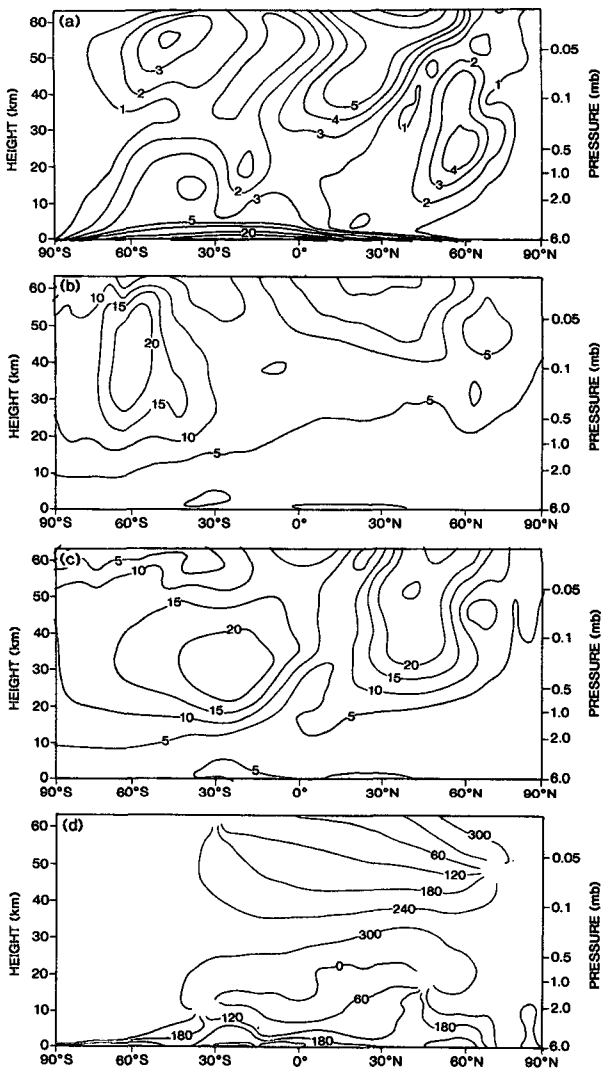

FIG. 16. Results for the westward propagating wave-1 component of the tide in the NH winter (L_s = 270) experiment with τ = 0.3 and the idealized wave-2 topography. Results for (a) temperature amplitude (contour labels in °K), (b) zonal wind amplitude (contour labels in m s^{-1}), (c) meridional wind amplitude (contour labels in m s^{-1}), and (d) zonal wind phase (degrees). Results are plotted as a function of the modified sigma coordinate, so the pressure scale is approximate below 2 mb.

dominant wavelength ~30 km. These basic features for $S_1(T)$ have been seen in classical tidal theory calculations of the terrestrial tide (e.g., Chapman and Lindzen 1970) and reflect that the tropical response is dominated by Hough modes associated with vertical propagation, while the high-latitude response is dominated by vertically trapped modes. In the present case the region of phase propagation extends significantly into the winter hemisphere, consistent with the modification of the classical theory expected from the presence of strong mean westerlies. A similar effect has been found in linear terrestrial tidal calculations that include realistic solstitial mean winds (Hagan et al. 1995). However, the deviations from the classical result are more pronounced in the present simulation. The relative Doppler shifts of the tides by the mean winds are expected to be larger on Mars since the zonal phase speed of the sun-synchronous tide is roughly one-half that on the earth. These deviations could be expected to significantly affect the calculations of the tidal forcing of the zonal-mean circulation as reported by Hamilton (1982), Zurek (1986), and Zurek and Haberle (1988).

Just as the case for $S_1(T)$, the region of significant vertical phase propagation for the sun-synchronous component of $S_1(u)$ is confined to the Tropics at low altitudes and tilts significantly into the winter hemisphere at higher altitudes (Fig. 16d). The amplitudes of both $S_1(u)$ and $S_1(v)$ also display significant hemispheric asymmetry.

The results for the sun-synchronous tides in an equinoctial simulation have also been examined (not shown). Not surprisingly, the tides at equinox are much more symmetric between the hemispheres. At low latitudes, the temperature and zonal wind amplitudes of the vertically propagating tide grow with height more rapidly than in the solstitial case. It is interesting that in the solstitial simulation, increasing the thermotidal excitation (by raising τ) actually lowers the height of the maximum tidal amplitude in the tropical winter hemisphere (where the vertically propagating tide is prominent). For optical depth τ = 1, the maximum amplitude of the vertically propagating diurnal thermal tide is at roughly 40 km. This suggests that the growth of the vertically propagating diurnal tide could be limited by some kind of breaking mechanism operating in the winter hemisphere [the possibility of tidal gravitational breaking has been discussed by Zurek (1976)].

In contrast with the tropical results, the diurnal tide in the extratropics was found to increase in amplitude with increasing aerosol. This difference in behavior is expected since S_1 at high latitudes is largely nonpropagating. Diurnal tidal temperatures at 0.5 mb (roughly 25 km in height) may be compared with those deduced by Martin and Kieffer (1979) from IRTM data following the 1977a (L_s = 226) and 1977b (L_s = 290) global dust storms. Simulated tidal temperatures at this level have maxima in the extratropics for optical depths greater than 0.3. Maximum temperature amplitudes of 7.5 and 12.5 K at 40°S were obtained in the τ = 1 and τ = 2 solstice simulations, respectively, which compare very well with the IRTM observations around this time. The τ = 2 simulation amplitudes are also consistent with the IRIS observations reported by Hanel et al. (1972) for the period corresponding to the 1971 global dust storm. The simulated tidal amplitude for L_s = 200 with τ = 2 had a maximum amplitude of 15 K at 65°S in very good agreement with the IRTM data following the 1977a dust storm.

Figure 17 shows the same quantities as Fig. 16 but for the simulated eastward propagating wave 1 component of the diurnal tide. In the lower atmosphere the zonal velocity has an equatorially trapped structure and the amplitude of $S_1(v)$ is considerably weaker than for $S_1(u)$. Both these features are expected for a classical Kelvin mode. Above about 20 km, significant deviations from the predictions of classical theory are evident, notably a tilt of the temperature and zonal wind amplitude maxima into the winter hemisphere. Analysis of additional simulations show considerable sensitivity of the Kelvin wave response in the upper atmosphere to the mean wind profile at low latitudes. In particular, when the region of westerly shear above the peak easterly jet is sufficiently strong (see Fig. 6), the Kelvin wave temperature response can actually shift into the summer hemisphere above 60 km.

For this low dust case, the strength of the simulated diurnal sun-synchronous and Kelvin modes in the ~5–40-km height range appear to be of very roughly the same magnitude. This means that a prediction of the diurnal range of temperature at a particular location (something that could conceivably be measured from orbiting spacecraft) requires a credible simulation of the structure of both the sun-synchronous and Kelvin wave components. When simulations with significantly larger dust amounts are analyzed, however, the temperature perturbation associated with the sun-synchronous diurnal tide does clearly dominate that of the eastward propagating Kelvin wave, particularly in the summer hemisphere.

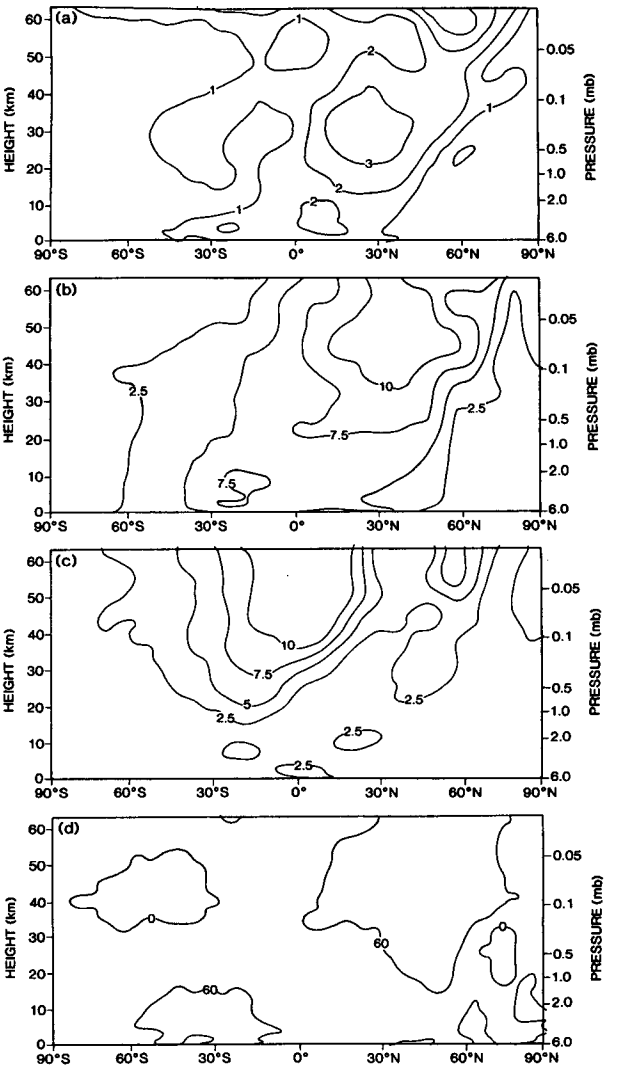

FIG. 17. As in Fig. 16 but for the eastward-propagating wave-1 component of the tide.

c. *Some more realistic calculations and the seasonal and interannual variation of surface tides*

A number of 40-sol simulations have been carried out with the L40 model employing realistic topography, surface thermal inertia, and albedo. Unless otherwise noted, the calculations to be described here used the horizontally uniform aerosol mixing ratio [see Eq. (4.1)]. Results will be presented for various times in the Martian year and for several dust optical depths. A number of these simulations were repeated with the L16 model, and very similar (within a few percent) results were obtained for the surface tides. In addition, the L16 model has been used in a simulation of a Martian annual cycle but with the progression of the solar declination and planetary orbital radius speeded up so that the entire annual cycle spans 300 sols, rather than the 668 sols in the actual Martian year. This was conducted with the $\tau = 0.3$ uniform dust distribution.

1) SUN-SYNCHRONOUS TIDES

Figure 18 shows the simulated amplitudes and phases of the sun-synchronous components of $S_1(p)$ and $S_2(p)$ during NH winter solstice for optical depths of 0.3, 1, and 2. The tidal pressure oscillations increase in amplitude in response to the stronger effective thermotidal forcing caused by increasing the total dust column. The sun-synchronous component $S_2(p)$ responds more strongly than $S_1(p)$ to increases in the vertically extended dust heating, in agreement with the expectations of classical theory (section 2).

Figure 19 is similar to Fig. 18 but presents results for $\tau = 0.3$ simulations near equinox and near the summer and winter solstices. A striking feature seen in this figure is the strong interhemispheric asymmetry in both $S_1(p)$ and $S_2(p)$. Simulations using the idealized (hemispherically symmetric) topography discussed in section 6b, or no topography at all, yield amplitudes for $S_2(p)$ that are stronger in the winter hemisphere than in the summer hemisphere in response to the meridional gradients in the mean state. By contrast, in the full

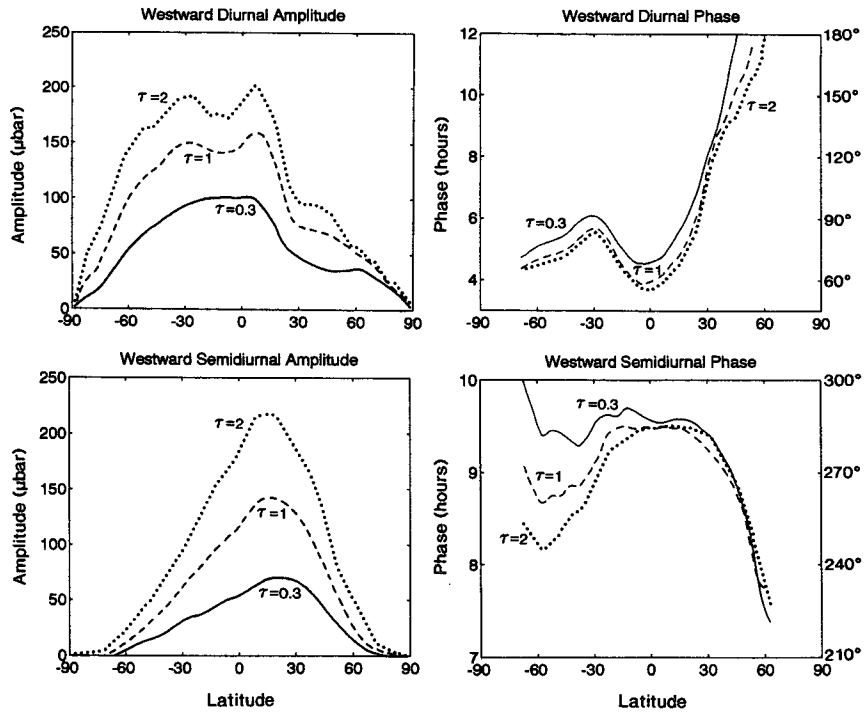

FIG. 18. Amplitudes and phases of the westward propagating components of $S_1(p)$ and $S_2(p)$ for NH winter (L_s = 270) with realistic topography. Results for three values of τ.

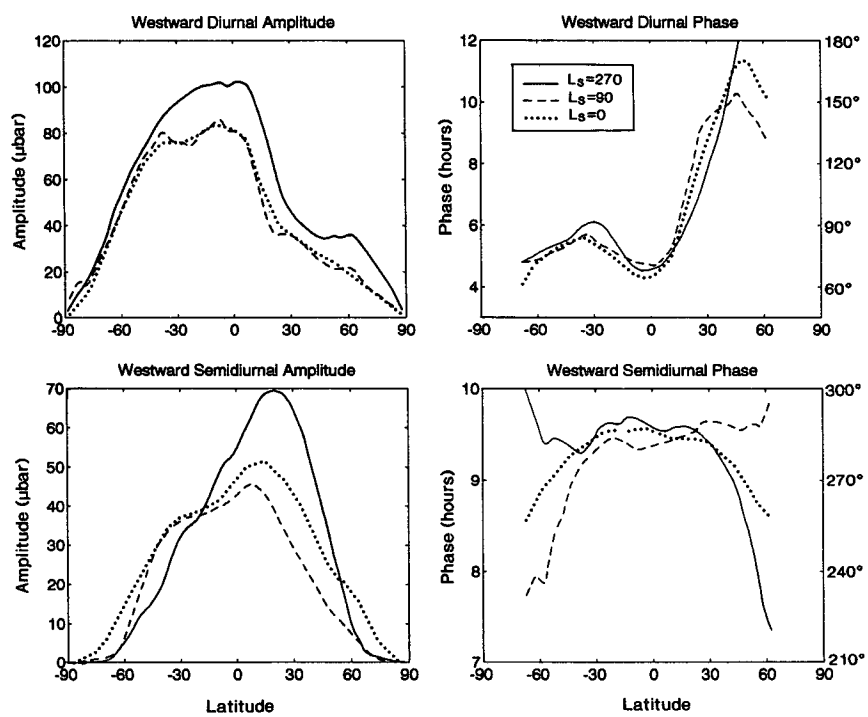

FIG. 19. Amplitudes and phases of the westward propagating component of $S_1(p)$ and $S_2(p)$ for optical depth τ = 0.3 for equinox, summer, and winter solstice.

calculation results shown in Fig. 19, the sun-synchronous $S_2(p)$ is strongest in the NH in all seasons. The larger $S_2(p)$ response in the NH may be explained simply as the consequence of the greater mean pressure and hence (with the present specification of dust concentration) larger total column of dust heating.

Figure 19 shows that there is also hemispheric asymmetry in both amplitude and phase of $S_1(p)$ that persists for all seasons. In this case, the larger amplitudes and earlier phases are found in the Southern Hemisphere. The topographic effect on $S_1(p)$ may be rather subtle, since much of the diurnal heating excites motions that are largely rotational (e.g., the wind field associated with the gravest antisymmetric Hough mode in classical theory is completely rotational). Such motions have small surface pressure signatures, a situation that may change markedly when the steep slope of the zonal-mean topography is included. In the case of flat topography, the velocity response is dominated by the symmetric components (at least equatorward of about 45°), even for significantly asymmetric heating. It will be shown below that in the full model simulation, the diurnal v field near the surface has a significant cross-equatorial component with upslope (i.e., predominantly southward) winds in the afternoon.

Figure 18 shows that as the effective depth of atmospheric heating increases due to increasing dust loading, the phase of the sun-synchronous component of $S_1(p)$ tends to advance. Classical theory predicts such an advance to be confined to the Tropics, but in the simulation, the phase advance is evident over a much broader region. Figure 19 shows that at the latitude of VL1 (22.5°N), the phase of the simulated sun-synchronous component of $S_1(p)$ is earliest during NH winter and latest in the NH summer. The actual observations of the phase of $S_1(p)$ at VL1 (Fig. 1) show the opposite seasonal evolution. Indeed, the observed phases of $S_1(p)$ during NH summer at both lander latitudes are much earlier than either the present simulations of the sun-synchronous component or classical theory would suggest [that is, near 0600 phase of $S_1(p)$ throughout the midlatitudes, in response to heating that peaks at noon].

Figures 18 and 19 show that the phase of the simulated sun-synchronous component of $S_2(p)$ at low latitudes changes less than $^1/_3$ h with season and dust loading. This is consistent with the expectations of classical tidal theory and with terrestrial observations. The actual phase of $S_2(p)$ at VL1 is observed (Fig. 2) to behave very differently, with a relative retardation of ~2 h as the season progresses from NH autumn through winter and spring, followed by an advance from NH summer back to autumn. At the VL2 latitude, the modeled phase is in reasonable agreement with the observed phase during NH autumn through early winter. However, the rather late phases observed during NH spring and summer are not accounted for by the sun-synchronous component of $S_2(p)$ alone.

2) OTHER COMPONENTS

Table 1 lists the meridionally averaged (60°S–60°N) surface pressure amplitudes of the eastward and westward propagating components of $S_1(p)$ by zonal wavenumber. Results are shown for four different seasons. This can be compared with the same analysis for the observed terrestrial $S_1(p)$ presented by Haurwitz (1965). The sun-synchronous component is obviously prominent in all seasons in Table 1 but it is less dominant than in the terrestrial atmosphere (where Haurwitz shows that the sun-synchronous component is roughly an order of magnitude larger than any other component). In all cases the largest non-sun-synchronous component is the eastward propagating wave 1, which can be identified with the diurnal normal-mode Kelvin wave. This Kelvin wave is particularly strong in early NH summer, when it is actually larger than the sun-synchronous tide. However, during the equinoctial seasons, the Kelvin wave is not so dominant. In fact, during these times, the diurnal eastward propagating zonal wavenumber 2 and 3 components are at least of comparable strength to the Kelvin wave at the latitudes of the Viking Landers.

For each experiment, the geographical distribution of the amplitude of $S_1(p)$ (i.e., equivalent of Fig. 9a) was plotted. In all cases, these figures show a prominent zonal wavenumber 2 pattern, although the strength of this wave 2 modulation varied among the individual experiments. For example, a maximum normalized amplitude of 0.06 was obtained in the NH winter ($L_s = 270$), $\tau = 2.0$ simulation. Except during NH summer, there is also a prominent local maximum in $S_1(p)$ associated with the Hellas basin.

Table 2 shows the harmonic analysis for the same four integrations but now applied to $S_2(p)$. The semidiurnal tide is dominated by the sun-synchronous component, but the eastward propagating wave 2 is also quite significant, particularly in NH summer. Again, this is in strong contrast to the situation in the terrestrial

TABLE 1. The amplitude of the diurnal surface pressure oscillation resolved into zonal wavenumbers. Amplitudes are averaged between 60°S and 60°N. Results for eastward propagating waves 1–4 (E1–E4), wavenumber 0, and westward propagating waves 1–4 (W1–W4). Results for four different integrations. The amplitudes are in μbar.

	$L_s = 30$ $\tau = 0.3$	$L_s = 100$ $\tau = 0.3$	$L_s = 200$ $\tau = 1$	$L_s = 270$ $\tau = 1$
E4	4.5	7.0	7.4	7.7
E3	8.5	10.7	15.9	14.0
E2	17.6	7.6	28.2	20.5
E1	31.9	98.8	34.8	59.6
0	6.3	7.5	12.4	16.2
W1	59.4	58.5	106.7	119.7
W2	6.3	5.1	13.2	12.6
W3	10.2	9.0	16.9	16.8
W4	5.0	5.2	9.6	11.3

TABLE 2. As in Table 1 but for the semidiurnal surface pressure oscillation.

	$L_s = 30$ $\tau = 0.3$	$L_s = 100$ $\tau = 0.3$	$L_s = 200$ $\tau = 1$	$L_s = 270$ $\tau = 1$
E4	1.2	2.3	2.5	2.6
E3	1.7	1.6	2.9	2.3
E2	11.0	27.8	8.8	15.0
E1	3.2	3.7	5.7	6.6
0	1.5	3.3	4.9	5.1
W1	6.7	9.4	8.3	8.5
W2	37.6	31.5	89.2	88.2
W3	2.5	1.9	5.3	5.2
W4	3.7	3.0	9.1	9.1

atmosphere where a similar analysis of surface pressure observations shows no particular prominence in the eastward wave 2 component (Kertz 1956).

The seasonal evolution of the amplitude and phase of the diurnal Kelvin mode in the $\tau = 0.3$ L16 "annual cycle" experiment is displayed in Fig. 20. These values were calculated from overlapped 2-day segments of hourly surface pressure data. The individual points in this figure show the same quantities for the shorter period L40 simulations, which employ various dust distributions (the results for $\tau = 0.3$ L40 simulations are not shown since they are very close to those in the L16 integration). The strongest Kelvin mode response occurs during the NH summer season, in agreement with the idealized calculations discussed earlier (e.g., Fig. 14). For the uniformly mixed dust case in summer, the simulated Kelvin wave amplitude is relatively insensitive to the amount of atmospheric aerosol present, although there is a distinct sensitivity of the phase on dust loading. In the other seasons the Kelvin response is actually a little stronger for larger optical depths. Evidently, the stronger thermotidal excitation from the increased dust can compensate for the effects of change in the mean temperature on the resonant response.

3) DETAILED COMPARISON WITH VIKING LANDER OBSERVATIONS

The amplitudes and phases of $S_1(p)$ and $S_2(p)$ in the L40 simulations at the model grid points nearest the VL1 and VL2 sites are presented in Figs. 21 and 22. The discussion will initially be confined to the simulations with the standard prescribed dust distribution and standard treatment of dust optical properties. These results can be compared with the time series of actual Viking observations of the same quantities shown in Figs. 1 and 2. Overall, there is a reasonable degree of agreement between the simulations and observations, particularly when the observations during NH autumn and winter dust storm periods are compared with the $\tau = 2$ simulations, while the rest of the observations are compared with the $\tau = 0.3$ model results. The simulations are notably successful in capturing the advance of the $S_1(p)$ phase from NH spring into summer and the subsequent retardation in the autumn. This advance is attributable to the presence of the Kelvin wave. This effect is shown in Fig. 12a. Because the two Viking Landers sites are almost exactly 180° apart, there is similar phase behavior at the two sites at this time when the Kelvin mode is especially prominent. The model suggests that the seasonal behavior of the phase of $S_1(p)$ at other longitudes would be more dramatic. The simulated phase of $S_1(p)$ at VL1 during NH spring is somewhat later than observed. The agreement with observations at this season could be improved if the model produced a somewhat stronger Kelvin wave, although note that the simulated results are strongly influenced by wave-2 and wave-3 diurnal tidal components as well. The observation that the $S_1(p)$ phase at VL2 is significantly later than 0600 hours (expected from classical theory at this extratropical location) over most of the year is also found in the simulations.

The simulated seasonal evolution of the phase of $S_2(p)$ at both landers is also in broad agreement with the observations, with both model and observations showing an advance from NH summer to autumn ($L_s = 90$ to $L_s = 180$) and a subsequent lag through winter

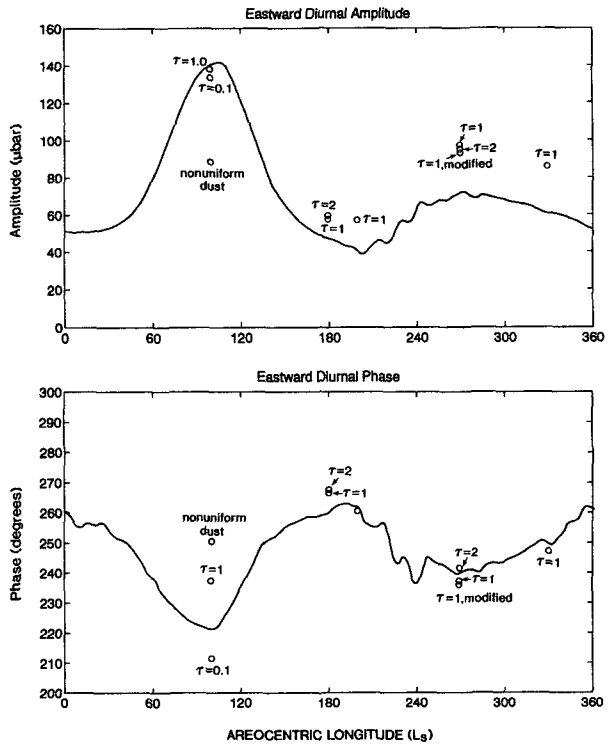

FIG. 20. The simulated diurnal Kelvin wave amplitude maximum plotted as a function of Martian season (areocentric longitude). The solid line is for the seasonal integration using uniformly mixed dust with total optical depth, $\tau = 0.3$. Circles are for results of experiments with other values of τ or some other modification. The bottom panel shows the corresponding time evolution of Kelvin wave phase.

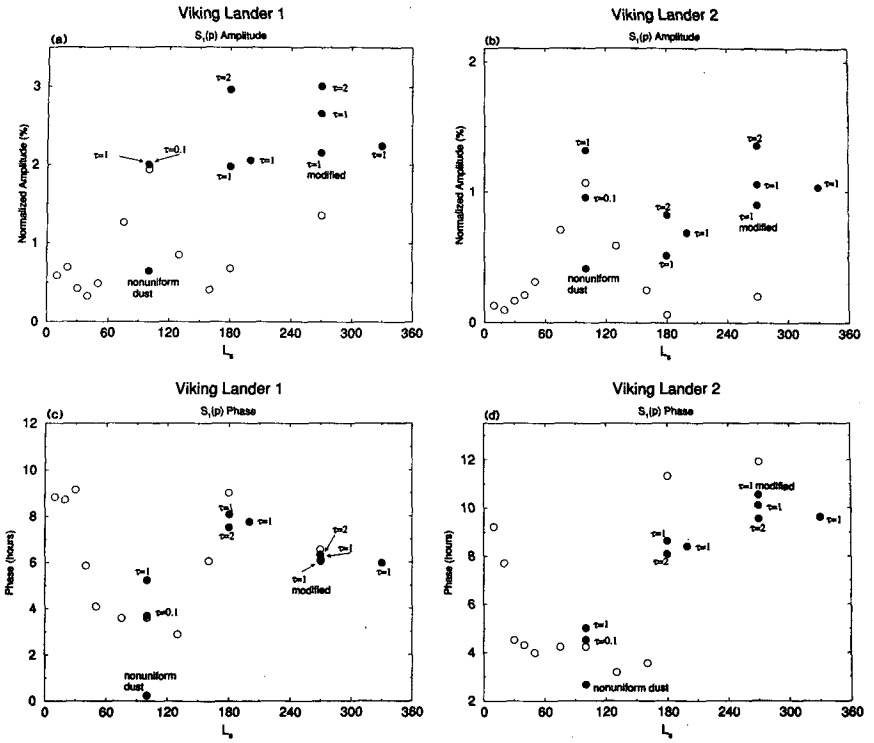

FIG. 21. The simulated amplitude (top) and phase (bottom) of $S_1(p)$ at the model grid point nearest the Viking Lander 1 site (left) and for the grid point nearest the Viking Lander 2 site (right). Results are expressed as functions of areocentric longitude. Amplitudes are normalized by the mean pressure and are expressed in percent. Each point represents results from a different experiment. The open circles were obtained from experiments using uniformly mixed dust with $\tau = 0.3$. The results obtained with other values of τ or some other modification are shown by the filled circles. See text for details.

into spring. As discussed previously, the observed late phases (later than 0940 hours) at some times in the annual cycle are not consistent with sun-synchronous tides alone. The presence of a semidiurnal Kelvin mode in the simulation brings the model results closer to those observed. The longitudinal variation in $S_2(p)$ associated with the interference of the eastward- and westward-propagating zonal wavenumber 2 components is such that the latest phases occur roughly at the longitudes of the two landers (see Fig. 12b). This zonal modulation is largest when the amplitudes of the two components are comparable. There are still some quite substantial differences between the simulations and observations, however. The simulated $S_2(p)$ phase at VL2 in the late winter remains earlier than 0900 hours, whereas the observations indicate that the phase becomes much later in late winter. At this time, the model result is closer to that expected from classical theory. During NH summer, the simulated $S_2(p)$ phases at VL1 are several hours later than observed. It seems reasonable to interpret these differences as evidence that the simulated semidiurnal Kelvin wave is unrealistically weak in NH winter and unrealistically strong in NH summer.

The simulated amplitudes of $S_1(p)$ and $S_2(p)$ change quite substantially as the prescribed dust opacity is varied over the range $\tau = 0.3$ to $\tau = 2$. Thus, it seems that observations and model results over most of the annual cycle could be brought into agreement with an appropriate choice of dust opacity. For example, the rather low values seen for the $\tau = 0.3$ simulation of tidal amplitudes in early NH spring could simply indicate that the actual mean optical depth at this time of year is somewhat greater than 0.3. However, there is one time of year when it is more difficult to explain the discrepancy between the simulated amplitudes and those observed. Near $L_s = 90$ (NH summer solstice) the $S_1(p)$ amplitudes in the $\tau = 0.3$ model results are at least twice as large as actually observed at both the VL1 and VL2 locations. There is a similar, though less serious, overprediction of amplitude of $S_2(p)$ at VL1. These problems persist even when the dust mixing ratio is reduced by a factor of 3 ($\tau = 0.1$). Much of the simulated diurnal tidal amplitude at the lander sites in this season is attributable to the resonant Kelvin mode, and this accounts for the relative insensitivity of the $S_1(p)$ amplitude to changing the global dust amounts. At lower dust levels, the reduced forcing for the Kelvin

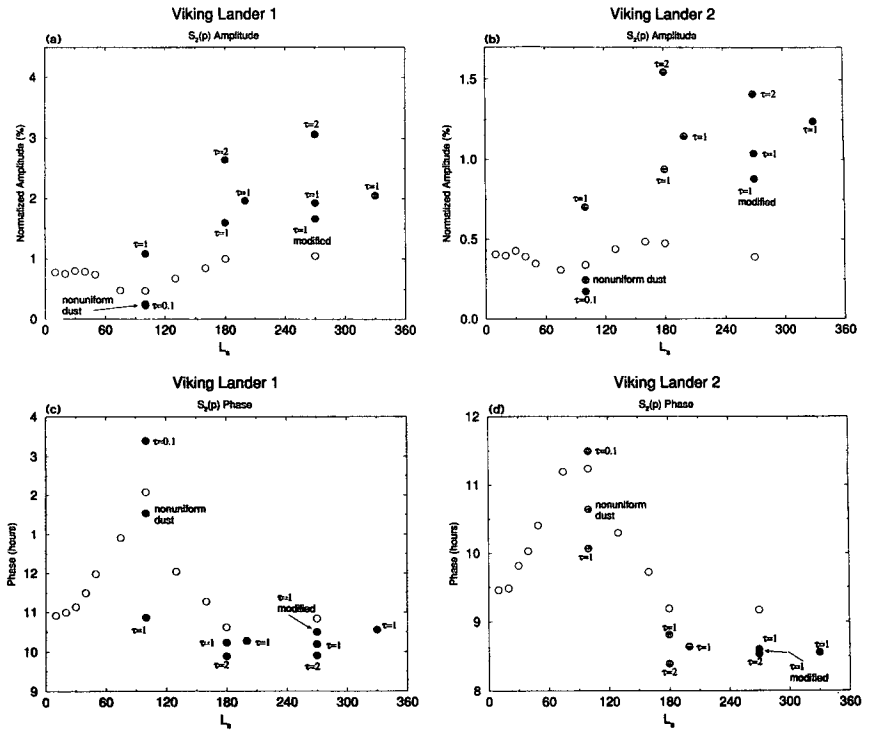

FIG. 22. As in Fig. 21 but for $S_2(p)$.

mode is offset by the enhanced resonance associated with the lower mean temperatures.

4) SIMULATIONS WITH NONUNIFORM DUST DISTRIBUTIONS

One possible explanation for the overly large amplitude Kelvin modes in the simulated northern summer season is that the geographical distribution of dust in the Martian atmosphere is not well represented by the "uniformly mixed" prescription used in the present standard experiments [Eq. 4.1]. The idealized calculations described in section 6b provide guidance on how the dust distribution could be modified so as to reduce the amplitude of the simulated Kelvin wave. In particular, it was shown that enhancing the thermotidal heating over highlands should produce a thermally forced Kelvin wave with the opposite phase of the (dominant) topographically forced wave, thus leading to a weaker Kelvin wave. This idea suggested a new simulation using the full model with an imposed nonuniform aerosol distribution. The dust distribution was modified by increasing the aerosol mixing ratio at low levels over highlands and decreasing it over lowlands so as to yield a more nearly horizontally uniform surface opacity with spatial variations on the order of 20% rather than 250%. The salient features of this distribution is shown in the top panel of Fig. 23, which represents the surface optical depth normalized with respect to a reference surface pressure of 6.1 mb (note that the present uniformly mixed distribution is just a constant when represented in this manner). The modified distribution in Fig. 23a would be reasonable if dust were preferentially raised or accumulated over highlands.

In a NH summer (L_s = 100) simulation employing the modified aerosol distribution, the amplitude of the diurnal Kelvin wave is reduced by 40% and the phase shifted eastward by 35° relative to the standard case. The amplitude response is consistent with the interpretation of a (partial) cancellation between the dust-induced forcing and the dynamical (topographical) forcing of the Kelvin wave. As expected, the sun-synchronous tides are relatively unaffected by the change in the aerosol distribution. The overall geographical distribution of $S_1(p)$ amplitude in the modified aerosol experiment (not shown) broadly resembles that for the standard case (Fig. 9). However, the tidal amplitudes and phases at the Viking lander sites are significantly changed from the standard experiment. These results are indicated in Figs. 21 and 22 by the points labeled "nonuniform dust." The unrealistically large $S_1(p)$ amplitudes in the standard experiment at both landers are markedly decreased in the nonuniform dust case. The phase of $S_2(p)$ has also moved into closer correspondence with observations. Much of the reduction in the amplitudes of $S_1(p)$ at the two lander sites can be ascribed to the decrease in Kelvin wave amplitude (and

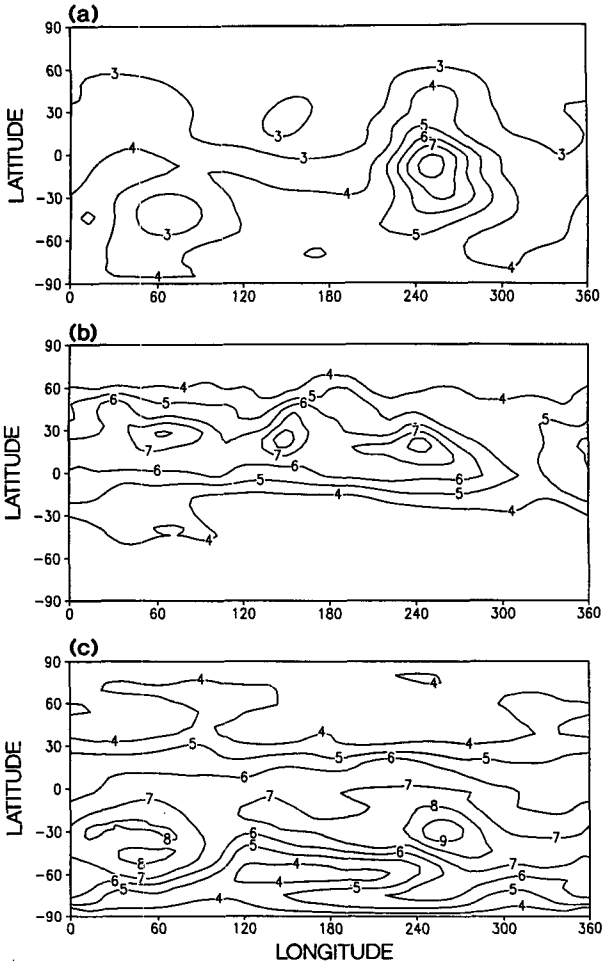

FIG. 23. Column optical depth normalized by the local surface pressure over the reference pressure. The contours have been multiplied by 10. (a) Imposed modified dust distribution. (b) Surface optical depth in the annual cycle interactive dust simulation during NH summer (L_s = 100). (c) Surface optical depth in the annual cycle interactive dust simulation during NH winter (L_s = 270).

shift in phase); however, there are also contributions from changes in the eastward propagating zonal wave 2 and 3 components. Since the amplitude of the Kelvin mode relative to its westward counterpart is considerably smaller in the other seasons, it seems reasonable that sensitivity to deviations from the uniformly mixed aerosol distribution would be less than during NH summer. This issue will be examined in a later section.

5) SENSITIVITY TO AEROSOL PARAMETERS

The aerosol optical properties employed will also influence the tidal simulations. The points labeled "modified" in Figs. 21 and 22 are for uniformly mixed τ = 1 simulations employing the aerosol scattering parameters suggested by Clancy et al. (1995). For a given absorber distribution, these parameters (increased single scattering albedo and reduced backscattering) tend to yield less radiative heating than the present standard parameters. The global mean temperature is about 8°C cooler than in the standard L_s = 270, τ = 1 experiment. The tidal surface pressure amplitudes of the tidal components are reduced by roughly 10% over the standard case, with somewhat larger reductions in $S_1(p)$ and $S_2(p)$ at the two lander sites. Simulations (not shown) of tidal amplitudes during NH summer using various aerosol optical parameters give evidence for the robustness of the Kelvin wave response at this time of the season. Again, weaker radiative heating leads to a cooler, hence more resonant, atmosphere, which compensates for the reduced tidal forcing.

d. Near-surface winds

Figure 24 shows the horizontal winds composited at 1600 local time minus those at 0400 local time at the lowest model level (~100 m) for a NH summer (τ = 0.3) simulation and for a NH winter (τ = 1) simulation, both carried out with the L40 model. A comparison with Fig. 7 shows that the diurnal winds are of comparable strength to the time-mean winds. There is an obvious influence of the topography on the diurnal winds (the sun-synchronous tide by itself would result in a zonally uniform distribution of local time winds). There is a tendency for late afternoon upslope (early morning downslope) winds over much of the surface.

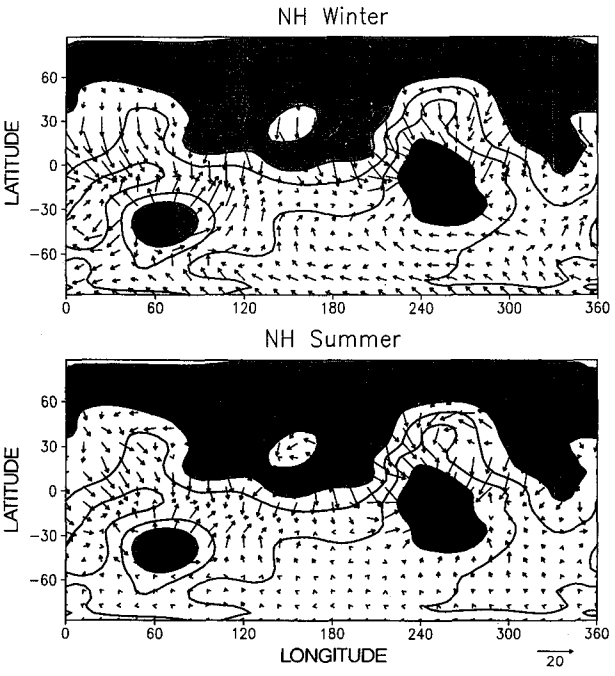

FIG. 24. The lowest model level wind field at 1600 local time minus that at 0400, for the simulations depicted in Fig. 7. The wind differences are multiplied by 0.5 so as to compare with the time-mean surface winds in Fig. 7.

A similar pattern holds for all seasons and dust distributions considered. Around a latitude circle, the local-time phase of $S_1(u)$ or $S_1(v)$ at the lowest levels can vary by as much as 10 h during NH winter (when the global-scale Kelvin wave is most strongly dominated by the sun-synchronous tide), an indication of the strong influence of the lower boundary. There are even larger phase variations in the zonal wind during NH summer, associated with the dominant Kelvin wave at this time. Tidal wind phase variations are closely correlated with the resolved variations in topographic slope. Examination of the comparable analysis from the 3° × 3.6° version of the L40 model reveals smaller-scale variability in the phase of the diurnal wind, which is again clearly correlated with the finer-scale topographical features.

While the results of the simulation support the view that local (i.e., grid-scale in the model) topography is important for determining the diurnal wind, there are still strong diurnal surface winds even in regions where the topographic slopes are weak, as well as regions where the 1600 minus 0400 wind vectors are nearly perpendicular to the topographic gradient. These deviations from pure afternoon upslope/morning downslope behavior are particularly pronounced in the summer hemisphere extratropics.

For optical depths of 1 and greater, the lowest level winds associated with the semidiurnal tide achieve amplitudes comparable to those of the diurnal tide. The semidiurnal wind oscillations are strongest poleward of ~40° and tend to show greater interhemispheric symmetry than the diurnal wind oscillations. The simulated semidiurnal wind fields are much more uniform with longitude than those for the diurnal tide, consistent with the expected domination of S_2 by the global-scale sun-synchronous components that are efficiently excited by vertically extended heating.

Hodographs showing the composite diurnal evolution of the simulated lowest level wind at the grid points closest to the VL1 and VL2 sites are presented in Fig. 25. Results are for NH winter solstice and for three different dust amounts. Note that these are winds for ~100 m above the surface, rather than at 1.6 m as observed by the Viking landers. In all cases, $S_2(u)$ and $S_2(v)$ have larger amplitude at VL2 than VL1, and the amplitude of the semidiurnal wind oscillation increases strongly with dust loading. The behavior of the simulated winds is in very good agreement with the observations at VL1 (Murphy et al. 1990) and VL2 (Leovy and Zurek 1979) for dust storm conditions. The nighttime loop of the VL2 semidiurnal oscillation is weaker than the daytime loop, as seen in the observations. This behavior might be anticipated if the near-surface winds become decoupled from the winds aloft as a very stable boundary layer evolves during the night. In the simulations, this difference becomes smaller for increasing optical depth.

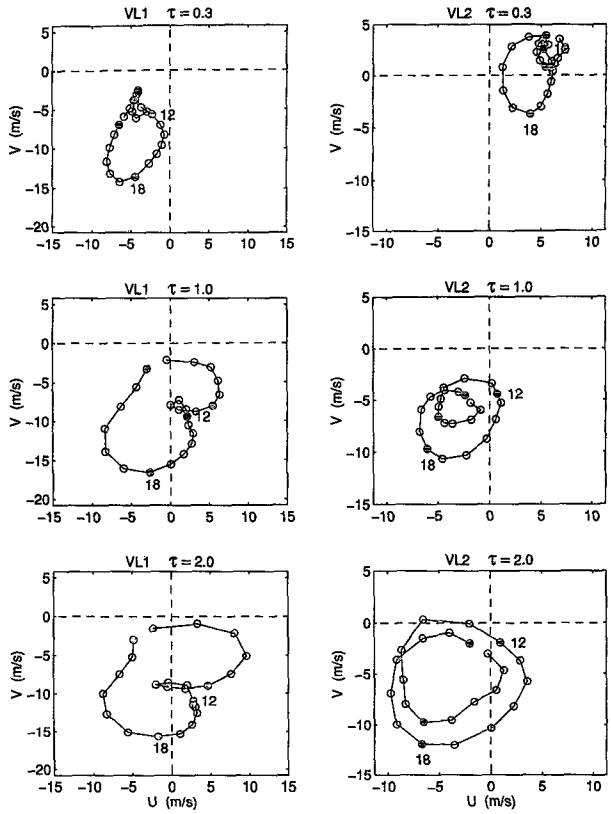

FIG. 25. Surface wind hodographs corresponding to VL1 (left) and VL2 (right) for three values of optical depth (τ = 0.3, 1.0, 2.0). The season is NH winter (L_s = 270). The wind axis values are in m s^{-1}.

The comparison of the simulated S_1 wind oscillation with the Viking observations is less satisfactory. While the overall clockwise rotation of the hodographs in Fig. 25 agrees with observations at this time of year, the phases of both $S_1(u)$ and $S_1(v)$ in the model are in poor agreement with those reported at VL1 and VL2 by Murphy et al. (1990). In early NH summer, both the observed and simulated diurnal hodographs (not shown) display a more linear polarization, with a dominant morning downslope-afternoon upslope character, although once again there are significant differences between the details of the daily surface wind evolution in the model and observations.

The comparison with the individual site observations is greatly complicated by the possible high degree of local topographic control over the diurnal wind. The results of the present simulations suggest that the topography right down to the smallest resolved scales in the 3° × 3.6° model has strong influence. It is certainly possible that even smaller-scale components of the topography are influencing the observed diurnal winds at VL1 and VL2 and that the agreement with model results would improve greatly if the model could be run at very high horizontal resolution. The diurnal modulation of turbulent mixing may also have a significant

effect on the phasing of the diurnal winds. However, as discussed in section 3, even models using the best estimate of the actual topographic slopes around the Viking sites have had very limited success in accounting for the observed diurnal wind oscillation (Savijarvi and Siili 1993; H93). It is not clear whether these problems result from the limitations of the simplified models employed or from inaccuracies in the estimate of the topography.

The diurnal and semidiurnal wind in the lowest few model levels tend to be very roughly parallel to those at the lowest level. Except at the lowest model level, the S_1 and S_2 winds are intensified in the lowest ~2 km near the ground. This surface intensification of winds is a well-known feature of classical tidal theory results for S_1 and S_2. Figure 26 presents a view of the vertical structure of $S_1(v)$ and $S_1(u)$ in the lower atmosphere of the model. In particular, this figure shows the latitude–pressure cross section of the amplitude of the diurnal meridional and zonal winds from a simulation employing zonally averaged topography and $\tau = 0.3$ (note that very similar results are obtained for the sun-synchronous components of $S_1(u)$ and $S_1(v)$ for simulations with realistic topography). There is a strong cross-equatorial flow in the lowest 2 km, with phase such that the northerly (i.e., upslope) flow peaks in the late afternoon. In simulations with full topography, the slope winds have comparably shallow vertical scales. In the absence of topography, the zonal and meridional diurnal tidal winds tend to be symmetric and antisymmetric, respectively, and have distinct, well-separated amplitude maxima at roughly 30°N and 30°S. This result has been greatly modified by the topography in the present model simulation.

During the NH autumn and winter seasons, the strongest simulated diurnal tidal winds in the Southern Hemisphere are located on the eastern flanks of the Tharsis plateau (Solis Planum) and north and west of the Hellas Basin. At the 1-km height level, these winds are locally in excess of 30 m s^{-1}. Total wind speeds at 1 km are in excess of 45 m s^{-1} at 30°S around the time of solstice. Such strong winds largely reflect the intense lower branch of the Hadley circulation. Following autumn equinox (L_s = 180–210), the Hadley circulation is relatively weak and, for $\tau = 1.0$, the tidal winds make up a large fraction of the low-level winds. Generally, the Kelvin wave makes a relatively small contribution to the near-surface winds (typically less than 3 m s^{-1}) due to its broad meridional scale.

The lowest level (~100 m) winds obtained in the present simulations are generally below the ~30 m s^{-1} threshold that has been estimated as necessary for the ~2 m winds to raise dust from the surface (Greeley et al. 1980). However, as has been noted above, at 1 km the model winds routinely exceed 30 m s^{-1} in some locations and times of the year. The model simulations lack the small-scale wind fluctuations that could produce localized mixing within the boundary layer and that could lead to gusts in which the surface wind speeds might become comparable to that of the wind aloft. Obviously characterizing such gustiness is a complicated problem, but the present model results suggest that a GCM will need a parameterization of this effect in order to self-consistently produce a dust storm.

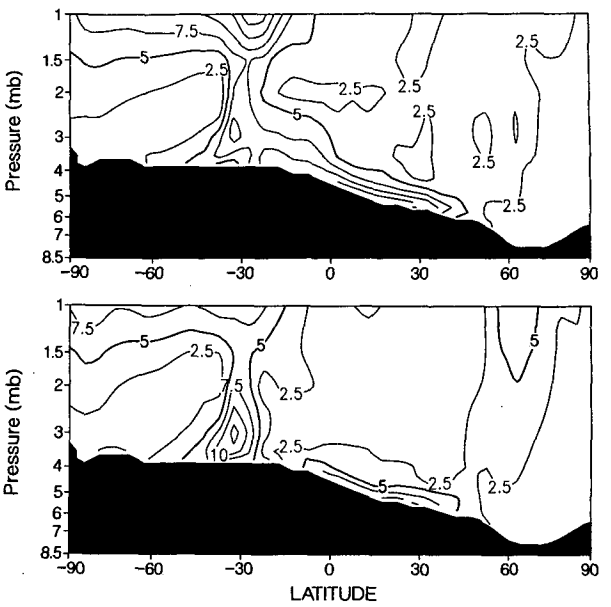

FIG. 26. Latitude–height plots of the amplitude of $S_1(v)$ (top) and $S_1(u)$ (bottom) for a NH winter simulation employing Martian zonal-mean topography: $\tau = 0.3$. Contour labels are in m s^{-1}. The vertical coordinate is pressure in mb.

e. *Interactive dust simulations*

A final set of L16 integrations was carried out to explore the tidal behavior in a version of the model with self-consistent dust advection (see section 4f for details). Axisymmetric calculations performed by Haberle et al. (1982) first demonstrated the importance of radiatively active aerosol. Two such integrations, using prescribed surface sources for the atmospheric dust, will be described here. The first is intended to approximate the onset of a major dust storm during NH winter. The second is intended to investigate the nature of the tidal response to the quasi-steady dust distribution that results from a constant, globally uniform dust source. Of specific interest is whether the model winds are able to "self-consistently" generate longitudinal variations in aerosol mixing ratio that would yield Kelvin wave behavior in closer accord with observation.

The standard uniformly mixed dust distribution with optical depth 0.3 was used as a fixed background aerosol in both experiments. A source of additional aerosol was introduced as a specified flux into the bottom model atmospheric layer. The first experiment did not include any sink for the atmospheric dust, while the

second integration did incorporate sedimentation of the dust (section 4f).

1) DUST STORM SIMULATION

This simulation extended for 60 days beginning from a standard $\tau = 0.3$ run at $L_s = 270$ (NH winter solstice). The modulation of the surface dust source is shown in Fig. 27a and features two major events initiated 0 and 30 days into the run. The dust source was a constant in the latitude belt 7.5° to 32.5°S and zero elsewhere. This range of latitudes is considered to be favored for sites of regional dust storms that evolve into planetary-scale dust storms at this season (Martin and Zurek 1993). The peak amplitude of the source is roughly a third of that used by Murphy et al. (1993) in earlier axisymmetric model calculations of the spread of global dust storms. The early stages of the "dust storm" are particularly interesting. Figure 28 shows an isosurface of aerosol mixing ratio averaged over sols 12–16 of the integration. In spite of the zonally uniform surface source, there are two very distinct dust plumes evident, one associated with the Tharsis Plateau and the other rising from the western slope of the Hellas Basin. Note that due to the large topographic relief, the optical depth at the surface is considerably larger in the Hellas Basin than elsewhere. The regions just west of the Hellas Basin (Hellespontus) and the southern part the Tharsis Plateau (Solis Planum) are the two associated with planet-encircling dust storms (Martin 1984). In the simulation, dust is advected southward from the source region by the lower branch of the Hadley cell, concentrated and lifted into the summer easterlies in zonally localized plumes and then is transported northward by the upper branch of the Hadley circulation. In the course of this integration, the global mean atmospheric optical depth, τ, increases from 0.3 to ~2.2 with an intermediate leveling off at $\tau \sim 1.3$.

Figure 27 summarizes a number of aspects of the evolution of the tidal fields in this simulation. All the tidal components shown have been calculated from overlapped 2-day segments of hourly ($1/24$ sol) data. Figure 27b shows the evolution of the maximum amplitude of the sun-synchronous component of $S_2(p)$, and illustrates the increasing dustiness of the atmosphere. The westward semidiurnal tide can be seen to be tending toward equilibration near days 30 and 60. The rapid rise in the amplitude of the sun-synchronous semidiurnal tide is similar to the increase of optical depth at the model grid points nearest the Viking Lander sites. At both sites, the rise time was roughly 10 and 6 days for the first and second events, respectively, with the surface optical depth increasing from roughly 0.3 to 2.5 in two distinct steps, just as for the $S_2(p)$ amplitude in Fig. 27b. The simulated optical depth behavior at the location of VL1 during the second "storm event" is comparably rapid but less intense than that actually observed during the 1977b dust storm (Murphy et al. 1993).

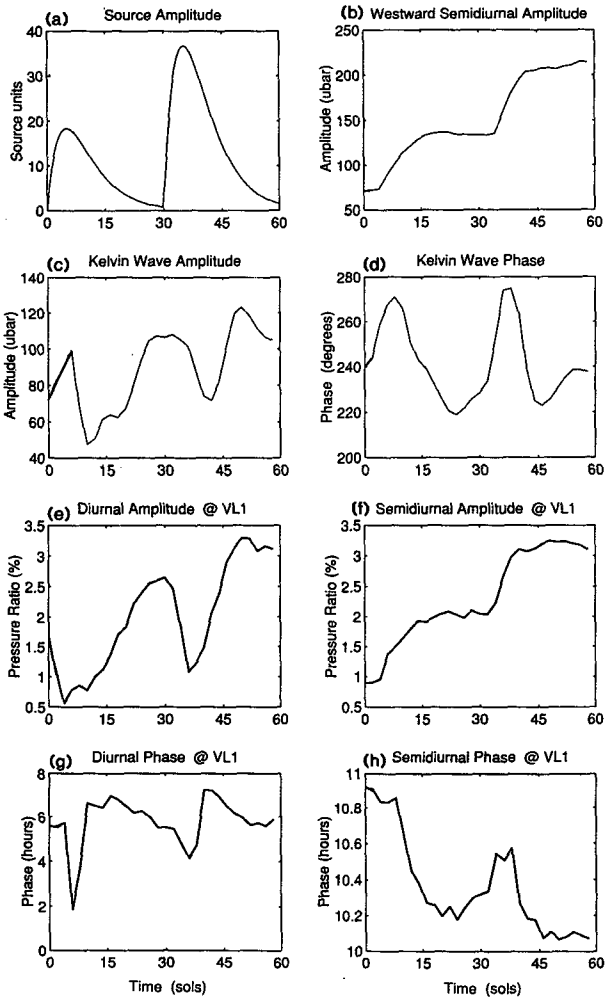

FIG. 27. Results from the NH winter dust storm simulation as described in the text. (a) The time evolution of the zonally uniform dust source representing two "events." The dimensions of the dust source are such that one source unit is equivalent to 2×10^{-9} kg m^{-2} s^{-1}. (b) The maximum amplitude of the westward component of $S_2(p)$ as a function of time. (c) The maximum amplitude of the eastward component of $S_1(p)$. (d) Phase of the eastward component of $S_1(p)$. (e) Amplitude of $S_1(p)$ normalized by the time mean pressure at the model grid point nearest the Viking Lander 1 site. (f) Amplitude of $S_2(p)$ normalized by the time mean pressure at the model grid point nearest the Viking Lander 1 site. (g) Phase of $S_1(p)$ at VL1. (h) Phase of $S_2(p)$ at VL1.

Figures 27c and 27d show the evolution of the diurnal Kelvin wave amplitude and phase. The rapid phase changes may be associated with the development of a zonally nonuniform aerosol distribution during times of maximum dust injection. The amplitude decrease and phase increase at the peak of each "storm" event is consistent with aerosol being concentrated over highlands as seen previously with the modified static dust distributions (e.g., section 6c.4).

The amplitude and phase of $S_1(p)$ and $S_2(p)$ at the grid point nearest the VL1 site are shown in Figs. 27e–

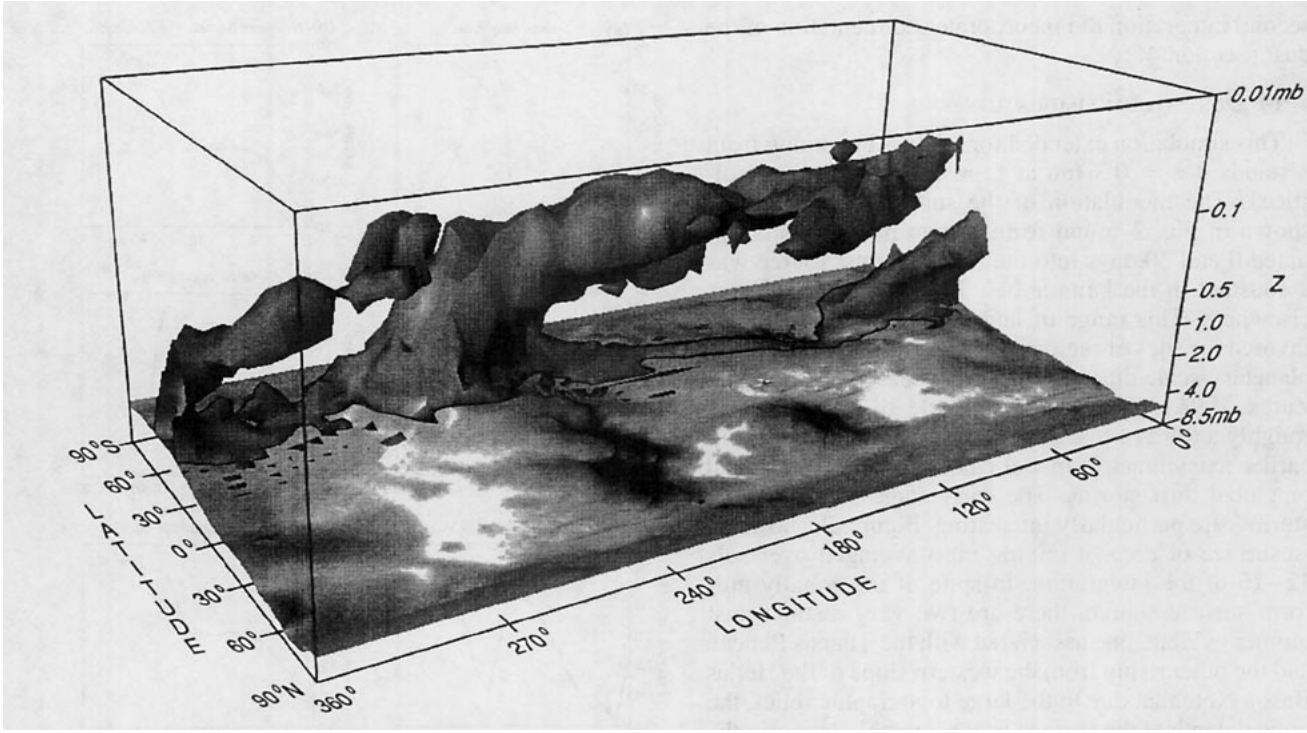

FIG. 28. Isosurface of aerosol mixing ratio for the initial stage of a NH winter dust storm simulation. The dust distribution is a 4-day average 12–16 days after initiation. The surface represents a mixing ratio yielding a column optical depth of unity if uniformly mixed. The data is displayed in a latitude–longitude projection with the northernmost latitude running along the front edge of the picture. The general upslope of topography from the NH to the SH is evident along the left edge of the picture. The smaller of the two dust plumes is rising up from the western slope of the Hellas Basin and continues into the Eastern Hemisphere as a distinct entity from the plume rising from the southern edge of the Tharsis plateau.

h. The behavior of the simulated $S_1(p)$ during the development of the second dust event starting at day 30 is quite similar to that actually observed at the onset of the 1977b major dust storm (near $L_s = 270$ in Fig. 1). In particular, there is a sharp amplitude decrease during days 30–35 followed by an increase over the following 10 days. These amplitude changes are accompanied by a phase lag during days 30–35 followed by a ~3-h phase advance over the next few days. During this period of strong dust injection, the simulated amplitude of $S_2(p)$ increases rapidly and there is an advance in phase, just as in the observations (Fig. 1). The spatial evolution of the surface optical depth, normalized to a constant reference pressure, indicates a relaxation toward a well-mixed dust distribution in the decaying stages of each "storm event." This process is particularly rapid in the zonal direction.

2) ANNUAL CYCLE EXPERIMENT WITH FIXED DUST SOURCE

The second simulation incorporated a steady globally uniform dust source much weaker than the peak source used in the dust storm experiment (5 units on Fig. 27a) and included the aerosol sedimentation. The integration was carried out for two Martian years of 300 sols (a factor of 2.2 speedup). The simulated seasonal cycles of $S_1(p)$ and $S_2(p)$ are very similar (within a few percent) in the two years, indicating that dust particle lifetimes are much shorter than the (shortened) annual period. Here, results are presented from the second year of the integration. The globally averaged aerosol opacity was about 0.5, including the fixed background dust. Panels b and c of Fig. 23 show the normalized surface optical depth for two times in the integration: one at NH summer solstice and the other for NH winter solstice. Dust plumes extended upward and westward from regions of strong east-facing slopes in the summer hemisphere in the manner noted in the discussion of the NH winter dust storm simulation. During NH summer, the prominent locations are the Tharsis Plateau, Elysium (130° long) and Syrtis Major (60° long). During SH summer, favored locations were the southern end of the Tharsis Plateau and the western Hellas Basin as described previously. It is noteworthy that for the same source strength, the dust plume rising from the southern end of the Tharsis Plateau during NH winter is considerably more intense than its NH counterparts during NH summer. Presumably this is a consequence of the stronger winds and more intense heating during SH summer, which are able to concentrate and loft aerosol more efficiently. The result is that a

plume during SH summer is more likely to penetrate higher into the atmosphere and have global influence than is the case during NH summer where the plumes have a more regional character.

The temporal behavior of the aerosol at two latitudes is summarized in Fig. 29. At both latitudes, the greatest deviations from uniform mixing occur during the summer season. The influence of Hellas and Tharsis is clearly seen in the left panel. The right panel shows that at the longitude of VL1 (312°), there are maxima in optical depth at $L_s = 50$ and 170 with a modest clearing tendency during summer as the aerosol is evidently preferentially advected toward the highlands to the west. Overall, the tendency for aerosol to be advected and concentrated over highlands (in the summer hemisphere) leads to a distribution of dust that deviates strongly from the standard "uniformly mixed" case and, in some respects, resembles the prescribed nonuniform case discussed in section 6c.4 (cf. Figs. 23a and 23b).

Figure 30 compares some aspects of the tidal response in this experiment with those of the L16 annual cycle simulation (with fixed, uniformly mixed aerosol) described in the previous section. The results are shown from late NH spring through autumn, the period that displays the least interannual variability in the observations. During NH summer, while the S_1 Kelvin wave amplitude in the interactive dust case differs little from that in the prescribed dust simulation (Fig. 30a), the phase is quite strongly modified (Fig. 30b). This leads to a much smaller (and more realistic) amplitude of $S_1(p)$ at VL1 in the interactive dust model (Fig. 30c). The early phase of $S_1(p)$ at VL1 relative to that expected from classical theory is evident in both simulations (Fig. 30e). The amplitude of $S_2(p)$ is enhanced in the interactive dust experiment, presumably due to the somewhat greater average optical depth (Fig. 30d). The phase for $S_2(p)$ is also changed considerably in the interactive dust case (Fig. 30f). In general, the NH summer VL1 results in the interactive experiment are somewhat more realistic than those in the prescribed dust case, although it seems that even better agreement with observations would be obtained by results somewhere between those of the two experiments. For example, the $S_2(p)$ amplitude is somewhat overpredicted and the $S_1(p)$ amplitude somewhat underpredicted in the interactive dust integration, which suggests further improvement could be achieved in an experiment with a somewhat weaker surface dust source. The results at VL2 (not shown) in the interactive dust case are also improved. As at VL1, the prominent peak in $S_1(p)$ at VL2 during summer solstice is markedly decreased in the interactive dust case relative to the uniformly mixed aerosol simulation.

This simulation demonstrates that rather realistic results for $S_1(p)$ during NH summer can be plausibly attained by allowing the model winds to advect the aerosol distribution. The steady dust source may be considered to represent the cumulative (stochastic) effect of small-scale transient dust raising events (dust devils) that could be expected to be widespread during the summer. For example, Ryan and Lucich (1983) have deduced the presence of numerous vorticial wind events (most common in spring and summer) from the VL1 and VL2 meteorological data. Thomas and Gierasch (1985) have reported the identification of dust

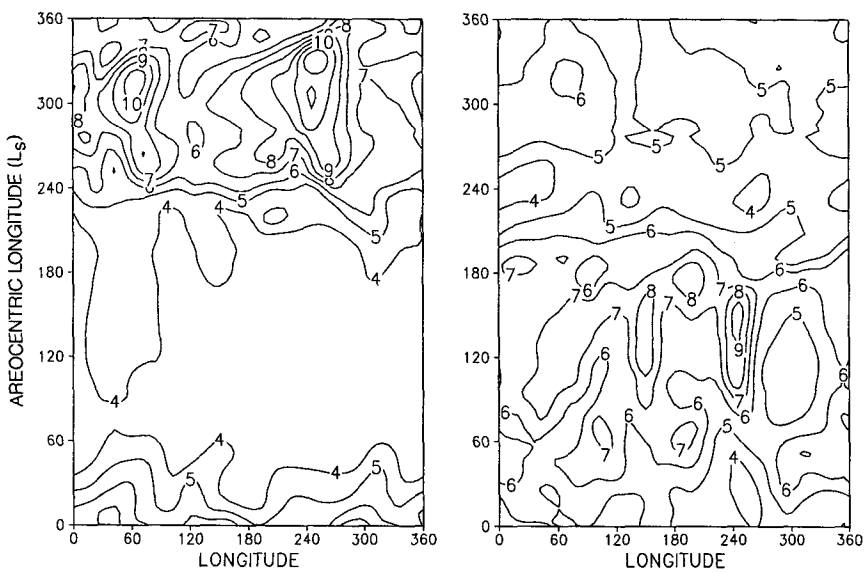

FIG. 29. Longitude–time plots of normalized column optical depth from the seasonal interactive dust simulation. The contours have been multiplied by 10. (a) Plot for latitude 32.5°S. (b) Plot for latitude 22.5°N.

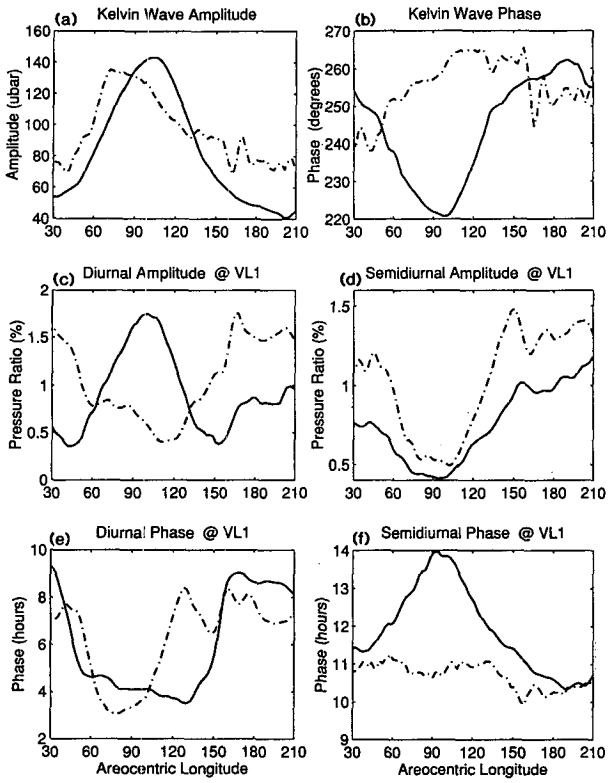

FIG. 30. Time series of tidal phases and amplitudes from the control and interactive dust experiments. (a) The maximum amplitude of the eastward component of $S_1(p)$. (b) Phase of the eastward component of $S_1(p)$. (c) Amplitude of $S_1(p)$ normalized by the time mean pressure at the model grid point nearest the Viking Lander 1 site. (d) Amplitude of $S_2(p)$ normalized by the time mean pressure at the model grid point nearest the Viking Lander 1 site. (e) Phase of $S_1(p)$ at VL1. (f) Phase of $S_2(p)$ at VL1.

devils with horizontal scales ~ 1 km in *Viking Orbiter* images. Such small-scale wind systems could play a significant role in the maintenance of the background aerosol level in the Martian atmosphere in the NH during this season. Of course, much of the dust injection into the atmosphere in the other seasons is probably due to baroclinic wave activity and other regional-scale events. The main point is that dust devil activity is most likely to be important as a local source of dust raising in the NH during the summer season. It is the altered heating due to the nonuniform transport of this aerosol that is responsible for the suppression of the Kelvin waves modes, yielding better agreement with Viking lander observations. Moreover, this activity would be expected to have little interannual variability, so long as the atmosphere remained relatively clear as has been observed.

There have been some limited attempts to deduce the longitudinal variations in dust concentration from observations. Drossart et al. (1991) report evidence that the total dust column is rather constant along the flanks of a Martian volcano. Such a result would imply considerably larger dust mixing ratios over higher terrain, in broad agreement with the present model results. Of course, the results of Drossart et al. are for horizontal scales somewhat smaller than actually resolved in the model. Chassefiere et al. (1995a,b) used solar occultation measurements to determine the aerosol opacity in the 15–25-km height range. They found no indication of longitudinal variability of aerosol. Their observations were obtained near equinox (L_s = 0–20) at a number of longitudes in the latitude range 0°–20°. This result is actually in reasonable agreement with the present model simulation, which produces a rather zonally uniform aerosol mixing ratio for these latitudes at this time in the Martian year.

7. Conclusions

This paper has described results from a newly developed comprehensive GCM of the Martian atmosphere. The basic features of the model simulation are in good overall agreement with those of the NASA Ames model (Pollack et al. 1990; H93) and the LMD model (Hourdin et al. 1993). In particular, simulations with comparable dust distributions yield similar zonal mean fields. Surface wind fields are comparable as well. One interesting difference with H93 is the greater tendency for tropical westerlies in the height range ~ 10–30 km in the present model. Most features of the diurnally averaged simulation in the present model appear to agree well with available observations. By far the most serious exception is the underestimated amplitude of the simulated transient waves at VL1.

Topography plays a fundamental role in determining the three-dimensional structure of the diurnally averaged winds in the model. Large-amplitude, nearly barotropic stationary waves are present up to high altitudes in the winter hemispheres (predominantly zonal wave 2 in the NH, and zonal wave 1 in SH). Stationary eddies are present in the Tropics as well and appear to be largely forced by thermal effects associated with the topography. The Hadley circulation is strongly affected by the thermal effects of zonal mean topography, so that during the SH summer, the winds of the surface branch are much stronger that those corresponding to NH summer (this is so even if the experiments are repeated keeping the solar insolation the same in both NH summer and SH summer). The Hadley cell is also strongly modulated in the zonal direction in the form of western boundary currents, most notably along the east-facing flanks of the Tharsis plateau. During SH summer there is strong large-scale ascent along the southern extent of the Hadley circulation with strongest ascent at the longitudes corresponding to Tharsis and the western part of the Hellas Basin. These topographically influenced large-scale circulations could be expected to have a major effect on aerosol transport.

This expectation is borne out in the two simulations described in section 6e, in which radiatively active

aerosol was advected by the model winds. Although axisymmetric surface dust sources were specified in these simulations, regional-scale redistribution of aerosol resulted, most notably in the form of plumes rising from the highlands near the subsolar latitude.

The presence of boundary inhomogeneities (particularly in topographic relief and surface thermal inertia) provides excitation of non-sun-synchronous tidal components. Prominent in the present simulations is the eastward propagating wave 1 diurnal Kelvin wave confirming the prediction of Zurek (1976). This wave is nearly resonant and thus easily excited, resulting in a surface pressure amplitude comparable to that of the sun-synchronous tide. The resulting interference between the two components yields a pronounced longitudinal modulation of both the amplitude and local time phase of the diurnal surface pressure oscillation. A near-resonant semidiurnal Kelvin wave is also strongly excited, and this appears even in the absence of the zonal wave 4 boundary inhomogeneities that would directly force it. In simulations without wave-4 boundary forcing, the amplitude of the semidiurnal Kelvin wave was shown to have a roughly quadratic dependence on the amplitude of the diurnal Kelvin wave. The importance of tidal nonlinearity in determining the observed daily variation of surface pressure is an unexpected result and certainly one with no terrestrial analog.

Several series of simulations were carried out to examine the resonant response of the Kelvin mode. In each series, the atmospheric temperature was varied by a specified offset while the tidal forcing was kept constant. These are analogs of the linear tidal theory calculations discussed by Zurek (1988). These experiments confirmed the earlier predictions that the Kelvin normal modes on Mars have natural frequencies close to the diurnal frequency (and its harmonics). At all seasons, the Martian atmosphere is predicted to be subresonant, so that increased atmospheric heating (either from orbital changes or increased dust loading) leads to a warmer and less resonant atmosphere. This has an interesting consequence for tidal simulations, since any effect that increases the atmospheric heating (more dust, higher solar insolation) leads to stronger direct tidal forcing but also to a mean state that pushes the Kelvin wave resonance farther from the diurnal frequency. These two effects can act to cancel each other and make the predicted Kelvin wave rather insensitive to the global dustiness of the atmosphere. In fact, during NH summer, the model predicts a remarkably small sensitivity of the Kelvin wave amplitude to variations in the total global-mean dust column employed (Fig. 20).

The model results for the diurnal and semidiurnal surface pressure oscillations were compared in detail with the observations at the two Viking lander sites. These observations were shown to be reasonably well simulated over much of the year with a globally uniform aerosol mixing ratio (as long as more total aerosol is employed in the northern winter season, when the largest dust storms are generally observed). There are features of the Viking observations that do not seem to be explainable in this way, however. In particular, in early northern summer, the model predicts amplitudes for the diurnal pressure oscillation at both lander sites that are much larger than observed. Also the phase of the simulated $S_2(p)$ at VL1 is a few hours later than observed. Much of the $S_1(p)$ amplitude at VL1 site at this time of year in the model is attributable to the Kelvin wave. It was also shown that the simulated $S_2(p)$ phase at VL1 was largely controlled by the strong S_2 Kelvin wave occurring in the NH summer simulation. As noted earlier, the simulated diurnal Kelvin wave is rather insensitive to the total dustiness, and this is reflected in the model results for the VL1 site as well. However, it was shown that the simulated diurnal Kelvin wave in the model can be weakened if the geographical distribution of aerosol is altered so that aerosol mixing ratios are largest over high topography. Such a dust distribution leads to a better prediction of the $S_2(p)$ phase at VL1 as well. Moreover, concentration of aerosol over highlands (at subsolar latitudes) is consistent with the simulated advective dust transport. The tidal pressure oscillations in the annual cycle interactive dust simulation were analyzed in detail and were found to reproduce rather well the seasonal evolution observed at VL1 and VL2, with the obvious exception of the times during global dust storms.

There has been a strong focus in this paper on the NH summer season because the Viking observations indicate strikingly little interannual tidal variability for this season. Moreover, the atmosphere is relatively clear during this season so that modeling results should be less subject to uncertainties due to regional-scale episodic dust storms. The simulations indicate that the diurnal pressure oscillations at the two landers are strongly dominated by the near-resonant Kelvin wave at this time, consistent with the observed anomalously early phase of the diurnal tides, which presumably is the signature of the dominant presence of a Kelvin mode. In this regard, it is interesting to note that Clancy et al. (1990, 1996) present evidence for a distinctly cooler (and presumably less dusty) atmosphere during the summers of the third and fourth Viking years than during the first two summers, whereas there is no indication of any significant change in the observed tides at VL1. Observations of $S_2(p)$ indicate a pronounced minimum at the time of NH summer solstice. This is a robust feature of the model simulations and is consistent with resonant enhancement of the semidiurnal Kelvin mode. It is also interesting to point out that later in the NH summer (L_s = 135–150) the increased variability of amplitude and phase of $S_1(p)$ and $S_2(p)$ discussed by Tillman (1988) occurs at a time when the Kelvin and sun-synchronous tides become comparable in amplitude.

The evolution of the observed $S_1(p)$ and $S_2(p)$ during the global dust storms is itself a rather interesting issue. Observations indicate a rather impressive brief drop in $S_1(p)$ amplitude at the onset of the 1977b storm, and at the onset of both the 1977a and 1977b storms, the phase of $S_1(p)$ at VL1 and VL2 displayed periods of rapid regression and progression. At least the qualitative behavior in the observations was captured in an interactive dust simulation in which a strong zonally uniform dust injection was prescribed in the SH Tropics and subtropics. The rapid ($\sim$ few days) response of the simulated tides in this experiment was largely a result of the rapid geographical organization of the dust by the model wind fields (Fig. 28). The simulation suggests a prominent role of the diurnal Kelvin wave in this process, as suggested by Zurek and Leovy (1981).

Both the annual cycle and "dust storm" interactive dust simulations show that a rather impressive amount of information about the atmosphere may be inferred from very limited tidal observations when used in conjunction with a sophisticated model. The details of the present model results for the effects of large-scale advective dust transport with the tides should be verifiable by future spacecraft missions. Particularly needed, of course, are more direct observations of the geographical distribution of atmospheric aerosol. Also a network of surface pressure observations, even just slightly expanded over that provided by the Viking mission, could provide valuable confirmation of the present tidal results.

While the present model does a rather good job of simulating available Viking observations of $S_1(p)$ and $S_2(p)$, the agreement of the daily cycle of the surface wind in the model with the VL1 and VL2 observations is less impressive, particularly for S_1. Examination of the global distribution of the S_1 wind field in the simulations provides some indication of the source for these difficulties. The $S_1(u)$ and $S_1(v)$ in the model appear to reflect a superposition of the global-scale tide and winds driven by topographic slopes (typically with strong upslope components in the late afternoon). The topographic slopes have an effect at all horizontal scales. The strong cross-equatorial diurnal winds seen in Figs. 25 and 26a are an example of global-scale slope winds associated with the topography. The importance of even rather small-scale topography was shown by results from experiments in which the model horizontal grid spacing was reduced to $\sim$150 km (section 6d).

The present model will be employed for additional investigations of Martian tidal dynamics. One issue that should be examined further is the nonlinear saturation of the diurnal tidal amplitude that apparently occurs at high levels (section 6b.4). This result in the present nonlinear model was anticipated by Zurek (1976), who predicted saturation of the diurnal tide at low latitudes due to local gravitational breaking. With further diagnostic analysis, the present model could be used to examine the importance of gravitational breaking and the effects it may have on vertical turbulent mixing and the tidal driving of the mean flow. The general issue of the tidal effects on the mean flow could also be further examined. Even below the breaking height, the eddy fluxes associated with the diurnal tide can be significant (Hamilton 1982; Zurek 1986). In the present full GCM, there is the possibility of self-consistent simulation not only of the tidal mean flow driving but also of the response of the rest of the circulation. One simple approach is to compare simulations performed with diurnally varying and diurnally averaged solar radiation. As noted in section 5a.2, preliminary comparisons of such integrations have suggested that the thermal tides play a significant role in forcing the equatorial superrotation seen in the region $\sim$ 10–30 km.

A final issue that needs to be mentioned, and one that connects many aspects of the Martian atmospheric modeling, is the generation of dust storms. As noted in section 6, the present results suggest that quite strong winds can be simulated at the lowest model level ($\sim$100 m), but if any simple (e.g., logarithmic) scaling were applied to the near-surface winds, the values right near the ground would be significantly weaker than the $\sim$30 m–s^{-1} value that is thought to be needed to raise significant amounts of dust. Clearly if a model is to be constructed that self-consistently generates a dust storm, some better treatment of the near-surface wind needs to be included. One approach that is now being pursued is to simply increase the vertical resolution in the model and include a more sophisticated closure scheme to account for vertical turbulent mixing. Whether this approach can produce the required results remains to be seen. It is quite possible that parameterizations that also consider the effects of horizontal inhomogeneities at subgrid scales will need to be developed. In any event, the present results certainly do emphasize the importance of topography in determining both the mean and tidal excursions of the surface winds.

Acknowledgments. The authors would like to thank Steven Lee for providing the raw VL1 and VL2 pressure data and Hans Vahlenkamp for assistance with the preparation of Fig. 28. The authors are also grateful to Brian Gross, Isaac Held, Jerry Mahlman, Richard Zurek, and the reviewers for their comments on the manuscript.

APPENDIX

Analysis of the Viking Lander Pressure Observations

Diurnal pressure composites were formed by assigning groups of 300 individual pressure observations into 24 "hourly" bins per sol. Detrending was carried out by removing the annual pressure signal. Typically, a diurnal composite represents a 3–4 sol interval of data,

with longer intervals during the fall and winter seasons in Martian years 3 and 4 at VL1. Intervals of length greater than 25 days were not considered nor were composites with any empty bins. The latter condition was relaxed for the diurnal composites for the time series at VL2 from late spring onward in the second year in which all had missing "bin" data (no more than 1 consecutive data gap) that were filled in with linear interpolation. These composites typically spanned intervals of 20 sols. The results are consistent with the more complete first year observations.

REFERENCES

Andrews, D. G., J. D. Mahlman, and R. W. Sinclair, 1983: Eliassen–Palm diagnostics of wave-mean flow interaction in the GFDL "SKYHI" general circulation model. *J. Atmos. Sci.*, **40,** 2768–2784.

——, C. B. Leovy, and J. R. Holton, 1987: *Middle Atmosphere Dynamics.* Academic Press, 489 pp.

Barnes, J. R., 1980: Time spectral analysis of midlatitude disturbances in the Martian atmosphere. *J. Atmos. Sci.*, **37,** 2002–2015.

——, 1981: Midlatitude disturbances in the Martian atmosphere: A second Mars year. *J. Atmos. Sci.*, **38,** 225–234.

——, B. B. Pollack, R. M. Haberle, C. B. Leovy, R. W. Zurek, H. Lee, and J. Schaeffer, 1993: Mars atmospheric dynamics as simulated by the NASA Ames General Circulation Model, 2. Transient baroclinic eddies. *J. Geophys. Res.*, **98,** 3125–3148.

Blumsack, S. L., P. J. Gierasch, and W. R. Wessel, 1973: An analytical and numerical study of the Martian planetary boundary layer over slopes. *J. Atmos. Sci.*, **30,** 66–82.

Briegleb, B. P., 1992: Delta–Eddington approximation for solar radiation in the NCAR community climate model. *J. Geophys. Res.*, **97,** 7603–7612.

Burk, S. D., 1976: Diurnal winds near the Martian polar caps. *J. Atmos. Sci.*, **33,** 923–939.

Chapman, S., and R. S. Lindzen, 1970: *Atmospheric Tides.* Reidel Publishing Co., 200 pp.

Charney, J. G., and P. G. Drazin, 1961: Propagation of planetary-scale disturbances from the lower into the upper atmosphere. *J. Geophys. Res.*, **66,** 83–109.

Chassefiere, E., P. Drossart, and O. Korablev, 1995a: Post–*Phobos* model for the altitude and size distribution of dust in the low Martian atmosphere. *J. Geophys. Res.*, **100,** 5525–5539.

——, S. W. Lee, G. R. Gladstone, W. W. McMillan, and T. Rousch, 1995b: A new model for Mars atmospheric dust based upon analysis of ultraviolet through infrared observations from *Mariner 9, Viking* and *Phobos. J. Geophys. Res.*, **100,** 5251–5263.

——, A. W. Grossman, M. J. Wolff, P. B. James, D. J. Rudy, Y. N. Billawala, B. J. Sandor, S. W. Lee, and D. O. Muhleman, 1996: Water vapor saturation at low altitudes around Mars aphelion: A key to Mars climate? *Icarus,* in press.

Clancy, R. T., D. O. Muhleman, and G. L. Berge, 1990: Global changes in the 0–70 km thermal structure of the Mars atmosphere derived from the 1975–1989 microwave CO spectra. *J. Geophys. Res.*, **95,** 14 543–14 554.

Conrath, B. J., 1975: Thermal structure of the Martian atmosphere during the dissipation of the dust storm of 1971. *Icarus,* **24,** 36–46.

——, 1976: Influence of planetary-scale topography on the diurnal thermal tide during the 1971 Martian dust storm. *J. Atmos. Sci.*, **33,** 2430–2439.

——, 1981: Planetary-scale wave structure in the Martian atmosphere. *Icarus,* **48,** 246–255.

——, R. Curran, R. Hanel, V. Kunde, W. Maguire, J. Pearl, J. Pirraglia, and J. Welker, 1973: Atmospheric and surface properties of Mars obtained by infrared spectroscopy on *Mariner 9. J. Geophys. Res.*, **78,** 4267–4278.

Drossart, P., J. Rosenquist, S. Erard, Y. Langevin, J. P. Bibring, and M. Combes, 1991: Martian aerosol properties from the *Phobos*/ISM experiment. *Ann. Geophys.*, **9,** 754–760.

Dunkerton, T. J., 1989: Nonlinear Hadley circulation driven by asymmetric differential heating. *J. Atmos. Sci.*, **46,** 956–974.

——, 1991: Nonlinear propagation of zonal winds in an atmosphere with Newtonian cooling and equatorial wavedriving. *J. Atmos. Sci.*, **48,** 236–263.

Fels, S. B., J. D. Mahlman, M. D. Schwarzkopf, and R. W. Sinclair, 1980: Stratospheric sensitivity to perturbations in ozone and carbon dioxide: Radiative and dynamical responses. *J. Atmos. Sci.*, **37,** 2265–2297.

Goody, R. M., and M. J. S. Belton, 1967: Radiative relaxation times for Mars. *Planet. Space Sci.*, **15,** 247–256.

Greeley, R., R. Leach, B. R. White, J. D. Iversen, and J. B. Pollack, 1980: Threshold wind speeds for sand on Mars: Wind tunnel simulations. *Geophys. Res. Lett.*, **7,** 121–124.

Haberle, R. M., C. B. Leovy, and J. B. Pollack, 1982: Some effects of global dust storms on the atmospheric circulation of Mars. *Icarus,* **50,** 322–367.

——, J. B. Pollack, J. R. Barnes, R. W. Zurek, C. B. Leovy, J. R. Murphy, H. Lee, and J. Schaeffer, 1993a: Mars atmospheric dynamics as simulated by the NASA Ames General Circulation Model 1. The zonal-mean circulation. *J. Geophys. Res.*, **98,** 3093–3123.

——, H. C. Houben, R. Hertenstein, and T. Herdtle, 1993b: A boundary-layer model for Mars: Comparison with Viking lander and entry data. *J. Atmos. Sci.*, **50,** 1544–1559.

Hagan, M. E., J. M. Forbes, and F. Vial, 1995: On modelling migrating solar tides. *Geophys. Res. Lett.*, **22,** 893–896.

Hamilton, K., 1982: The effects of solar tides on the general circulation of the Martian atmosphere. *J. Atmos. Sci.*, **39,** 481–485.

——, 1984: Evidence for a normal mode Kelvin wave in the atmosphere. *J. Meteor. Soc. Japan,* **62,** 308–311.

——, and R. R. Garcia, 1986: Theory and observations of the short-period normal mode oscillations of the atmosphere. *J. Geophys. Res.*, **91,** 11 867–11 875.

——, R. J. Wilson, J. D. Mahlman, and L. J. Umscheid, 1995: Climatology of the SKYHI troposphere-stratosphere-mesosphere general circulation model. *J. Atmos. Sci.*, **52,** 5–43.

Hanel, R., B. Conrath, W. Hovis, V. Kunde, P. Lowman, W. Maguire, J. Pearl, J. Pirraglia, C. Prabhakara, and B. Schlachman, 1972: Investigation of the Martian environment by infrared spectroscopy on *Mariner 9. Icarus,* **17,** 423–442.

Haurwitz, B., 1965: The diurnal surface pressure oscillation. *Arch. Meteor. Geophys. Biokl.*, **14,** 361–379.

Hess, S. L., R. M. Henry, C. B. Leovy, J. A. Ryan, and J. E. Tillman, 1977: Meteorological results from the surface of Mars: *Viking 1* and 2. *J. Geophys. Res.*, **82,** 4559–4574.

Hicks, B. B., 1976: Wind profile relationships from the Wangara experiment. *Quart. J. Roy. Meteor. Soc.*, **102,** 535–551.

Hirota, I., and T. Hirooka, 1984: Normal mode Rossby waves observed in the upper stratosphere. Part 1: First symmetric modes of zonal wave numbers one and two. *J. Atmos. Sci.*, **41,** 1253–1267.

——, and ——, 1985: Normal mode Rossby waves observed in the upper stratosphere. Part 2: Second antisymmetric and symmetric modes of zonal wave numbers one and two. *J. Atmos. Sci.*, **42,** 536–548.

Houghton, J. T., 1963: The absorption of solar infra-red radiation by the lower stratosphere. *Quart. J. Roy. Meteor. Soc.*, **89,** 319–331.

Hourdin, F., 1992: A new representation of the CO_2 15-micron band for a Martian general circulation model. *J. Geophys. Res.*, **97,** 18 319–18 335.

——, P. Le Van, F. Forget, and O. Talagrand, 1993: Meteorological variability and the annual surface pressure cycle on Mars. *J. Atmos. Sci.*, **50,** 3625–3640.

Joshi, M. M., S. R. Lewis, P. L. Read, and D. C. Catling, 1994: Western boundary currents in the atmosphere of Mars. *Nature,* **367,** 548–551.

——, ——, ——, and ——, 1995: Western boundary currents in the Martian atmosphere: Numerical simulations and observational evidence. *J. Geophys. Res.,* **100,** 5485–5500.

Kahn, R. A., T. Z. Martin, R. W. Zurek, and S. W. Lee, 1992: The Martian dust cycle. *Mars,* H. H. Kieffer, B. M. Jakosky, C. W. Snyder, and M. S. Matthews, Eds., 1017–1053, The University of Arizona Press, 1498 pp.

Kertz, W., 1956: Components of the semidiurnal pressure oscillation. New York University Dept. of Meteor. and Oceanogr. Sci. Rep. 4.

Kieffer, H. H., T. Z. Martin, A. R. Peterfreund, B. M. Jakosky, E. D. Miner, and F. D. Palluconi, 1977: Thermal and albedo mapping of Mars during the Viking primary mission. *J. Geophys. Res.,* **82,** 4249–4291.

Kurihara, Y., and J. L. Holloway, 1967: Numerical integration of a nine-level primitive equations model formulated by the box method. *Mon. Wea. Rev.,* **95,** 509–530.

Lellouch, E., J. Rosenqvist, J. J. Goldstein, S. W. Bougher, and G. Paubert, 1992: First absolute wind measurements in the middle atmosphere of Mars. *Astrophys. J.,* **383,** 401–406.

Leovy, C. B., 1981: Observations of Martian tides over two annual cycles. *J. Atmos. Sci.,* **38,** 30–39.

——, and Y. Mintz, 1969: Numerical simulations of the atmospheric circulation and climate of Mars. *J. Atmos. Sci.,* **26,** 1167–1190.

——, and R. W. Zurek, 1979: Thermal tides and Martian dust storms: Direct evidence for coupling. *J. Geophys. Res.,* **84,** 2956–2968.

——, ——, and J. B. Pollack, 1973: Mechanisms for Mars dust storms. *J. Atmos. Sci.,* **30,** 749–762.

——, J. E. Tillman, W. R. Guest, and J. R. Barnes, 1985: Interannual variability of Martian weather. *Recent Advances in Planetary Meteorology,* G. E. Hunt, Ed., Cambridge University Press, 69–84.

Levy, H., J. D. Mahlman, and W. J. Moxim, 1982: Tropospheric N_2O variability. *J. Geophys. Res.,* **87,** j3061–j3080.

Lindzen, R. S., 1970: The application and applicability of terrestrial atmospheric tidal theory to Venus and Mars. *J. Atmos. Sci.,* **27,** 536–549.

Longuet-Higgins, M. S., 1968: The eigenfunctions of Laplace's tidal equations over a sphere. *Philos. Trans. Roy. Soc.,* **A262,** 511–607.

Madden, R. A., 1978: Further evidence of traveling planetary waves. *J. Atmos. Sci.,* **35,** 1605–1618.

Mahlman, J. D., and L. J. Umscheid, 1987: Comprehensive modeling of the middle atmosphere: The influence of horizontal resolution. *Transport Processes in the Middle Atmosphere,* G. Visconti and R. Garcia, Eds., D. Reidel, 251–266.

Martin, L. J., 1984: Clearing the Martian air: The troubled history of dust storms. *Icarus,* **57,** 317–321.

——, and R. W. Zurek, 1993: An analysis of the history of dust activity on Mars. *J. Geophys. Res.,* **98,** 3221–3246.

Martin, T. Z., and H. Kieffer, 1979: Thermal infrared properties of the Martian atmosphere, 2. The 15 μm band measurements. *J. Geophys. Res.,* **84,** 2843–2852.

Murphy, J. R., C. B. Leovy, and J. E. Tillman, 1990: Observations of surface winds in the Martian subtropics. *J. Geophys. Res.,* **95,** 14 555–14 576.

——, R. M. Haberle, O. B. Toon, and J. B. Pollack, 1993: Martian global dust storms: Zonally symmetric numerical simulations including size-dependent particle transport. *J. Geophys. Res.,* **98,** 3197–3220.

Palluconi, F. D., and H. H. Kieffer, 1981: Thermal inertia mapping of Mars from 60 S to 60 N. *Icarus,* **45,** 415–426.

Pollack, J. B., D. S. Colburn, F. M. Flasar, R. Kahn, C. E. Carlston, and D. E. Pidek, 1979: Properties and effects of dust particles suspended in the Martian atmosphere. *J. Geophys. Res.,* **84,** 2929–2946.

——, C. B. Leovy, P. W. Greiman, and Y. Mintz, 1981: A Martian general circulation experiment with large topography. *J. Atmos. Sci.,* **38,** 3–29.

——, R. M. Haberle, J. Schaeffer, and H. Lee, 1990: Simulations of the general circulation of the Martian atmosphere 1: Polar processes. *J. Geophys. Res.,* **95,** 1447–1474.

——, M. E. Ockert-Bell, and M. K. Shepard, 1995: Viking Lander image analysis of Martian atmospheric dust. *J. Geophys. Res.,* **100,** 5235–5250.

Ryan, J. A., and R. D. Lucich, 1983: Possible dust devils, vortices on Mars. *J. Geophys. Res.,* **88,** 11 005–11 011.

Salby, M. L., 1981a: Rossby normal modes in nonuniform background configuration. Part I: Simple fields. *J. Atmos. Sci.,* **38,** 1803–1826.

——, 1981b: Rossby normal modes in nonuniform background configuration. Part II: Equinox and solstice conditions. *J. Atmos. Sci.,* **38,** 1827–1840.

——, 1984: Survey of planetary-scale waves: The state of theory and observations. *Rev. Geophys.,* **22,** 209–236.

Savijarvi, H., and T. Siili, 1993: The Martian slope winds and the nocturnal PBL jet. *J. Atmos. Sci.,* **50,** 77–88.

Seiff, A., 1993: Mars atmospheric winds indicated by motion of the Viking landers during parachute descent. *J. Geophys. Res.,* **98,** 7461–7474.

Thomas, P., and P. J. Gierasch, 1985: Dust devils on Mars. *Science,* **230,** 175–177.

Thompson, W., 1882: On the thermodynamic acceleration of the earth's rotation. *Proc. Roy. Soc. Edinburgh,* **11,** 396–405.

Tillman, J. E., 1988: Mars global atmospheric oscillations: Annually synchronized, transient normal-mode oscillations and the triggering of global dust storm. *J. Geophys. Res.,* **93,** 9433–9451.

Toon, O. B., J. B. Pollack, and C. Sagan, 1977: Physical properties of the particles comprising the Martian dust storm of 1971–1972. *Icarus,* **30,** 663–696.

Touloukian, Y. S., and T. Makita, 1970: Specific heat: Nonmetallic liquids and gases. *Thermophysical Properties of Matter 6,* Y. S. Touloukian, Ed., Plenum, 143–151.

U.S. Geological Survey, 1991: *Atlas of Mars.* Topographic Series, U.S. Geological Survey, M 15M, I-2160, 3 sheets.

Webster, P. J., 1977: The low-latitude circulation of Mars. *Icarus,* **30,** 626–649.

Zurek, R. W., 1976: Diurnal tide in the Martian atmosphere. *J. Atmos. Sci.,* **33,** 321–337.

——, 1980: Surface pressure response to elevated tidal heating sources: Comparison of earth and Mars. *J. Atmos. Sci.,* **37,** 1132–1136.

——, 1981: Inference of dust opacities for the 1977 Martian great dust storms from Viking Lander 1 pressure data. *Icarus,* **45,** 652–670.

——, 1986: Atmospheric tidal forcing of the zonal-mean circulation: The Martian dusty atmosphere. *J. Atmos. Sci.,* **43,** 652–670.

——, 1988: Free and forced modes in the Martian atmosphere. *J. Geophys. Res.,* **93,** 9452–9462.

——, and C. B. Leovy, 1981: Thermal tides in the dusty Martian atmosphere: A verification of theory. *Science,* **213,** 437–439.

——, and R. M. Haberle, 1988: Zonally symmetric response to atmospheric tidal forcing in the dusty Martian atmosphere. *J. Atmos. Sci.,* **45,** 2469–2485.

——, J. R. Barnes, R. M. Haberle, J. B. Pollack, J. E. Tillman, and C. B. Leovy, 1992: Dynamics of the atmosphere of Mars. *Mars,* H. H. Kieffer, B. M. Jakosky, C. W. Synder, and M. S. Matthews, Eds., The University of Arizona Press, 1498 pp.